



1 **Identifying Critical Input Parameters for Improving**
2 **Drag-Based CME Arrival Time Predictions**

3 **C. Kay^{1,2}, M. L. Mays¹, C. Verbeke³**

4 ¹Heliophysics Science Division, NASA Goddard Space Flight Center, Greenbelt, MD, USA

5 ²Dept. of Physics, The Catholic University of America, Washington DC, USA

6 ³Centre of Mathematical Plasma-Astrophysics, Department of Mathematics, Catholic University of
7 Leuven, Leuven, Belgium

8 **Key Points:**

- 9 • We study the sensitivity of drag-based arrival time models to input parameters
10 • Different precisions on the input parameters are needed for different “strength”
11 CMEs
12 • The arrival time tends to be more sensitive to CME parameters than solar wind
13 parameters

Corresponding author: C. Kay, christina.d.kay@nasa.gov

-1-

This article has been accepted for publication and undergone full peer review but has not been through the copyediting, typesetting, pagination and proofreading process which may lead to differences between this version and the Version of Record. Please cite this article as doi: 10.1029/2019SW002411

Abstract

Coronal mass ejections (CMEs) typically cause the strongest geomagnetic storms so a major focus of space weather research has been predicting the arrival time of CMEs. Most arrival time models fall into two categories: (1) drag-based models that integrate the drag force between a simplified CME structure and the background solar wind and (2) full magnetohydrodynamic (MHD) models. Drag-based models typically are much more computationally efficient than MHD models, allowing for ensemble modeling. While arrival time predictions have improved since the earliest attempts, both types of models currently have difficulty achieving mean absolute errors below 10 hours. Here we use a drag-based model ANTEATR (Another Type of Ensemble Arrival Time Results, Kay & Gopalswamy, 2018) to explore the sensitivity of arrival times to various input parameters. We consider CMEs of different strengths from average to extreme size, speed, and mass (kinetic energies between 9×10^{29} and 6×10^{32} erg). For each scale CME we vary the input parameters to reflect the current observational uncertainty in each and determine how accurately each must be known to achieve predictions that are accurate within 5 hours. We find that different scale CMEs are the most sensitive to different parameters. The transit time of average strength CMEs depends most strongly on the CME speed whereas an extreme strength CME is the most sensitive to the angular width. A precise CME direction is critical for impacts near the flanks, but not near the CME nose. We also show that the Drag Based Model (Vršnak et al., 2013) has similar sensitivities, suggesting that these results are representative for all drag-based models.

Plain Language Summary

Large explosions of plasma and magnetic field known as coronal mass ejections frequently erupt from the solar atmosphere. When CMEs head toward Earth they interact with the near-Earth plasma and magnetic field, affecting the “space weather.” CMEs typically cause the strongest space weather effects so a major focus has been predicting the time it takes for a CME to propagate from the Sun to the Earth. Many models have been developed over the past decades to predict the arrival time of CMEs but all have difficulty achieving absolute errors less than 10 hours. Here we use a simple model that integrates the drag force between a CME and the background solar wind. Due to the model’s simplicity we can run a large number of simulations, allowing us to explore how the arrival time changes as the various model inputs are changed. We consider CMEs of different strengths and find that the behavior differs between average and extreme CMEs. We determine the precision needed for each input parameter to achieve predictions that are accurate within 5 hours. We compare our results with those from a similar model. Both models exhibit the same sensitivity to the input parameters, suggesting that these results are representative for most drag-based models.

1 Introduction

Space weather refers to the state of the near-Earth radiation and plasma environment, which often changes as a result of solar-driven activity. Understanding the behavior of this environment is crucial as it can affect human technologies, both in space and on the Earth’s surface, and adversely affect the health of humans in space. The latter is of particular relevance given NASA’s renewed focus on human space exploration with a plan to return to the Moon by 2024 and eventually send humans to Mars.

Coronal mass ejections (CMEs) are large explosions of plasma and structured magnetic field that routinely erupt from the solar surface and continue propagating out through the solar system. CMEs drive some of the strongest space weather effects at Earth, so accurately predicting their arrival is essential.

62 Much focus has been placed on modeling the arrival time of CMEs and most mod-
63 els follow the same basic algorithm. First, a CME is observed remotely near the Sun and
64 its basic properties, such as speed, size, and direction of propagation, are reconstructed
65 using some sort of morphological model (e.g. Xie et al., 2004; Thernisien et al., 2006).
66 These parameters are then used in a transit model that describes the interaction between
67 the CME and the background solar wind through which it propagates. The duration de-
68 termined from the transit model is combined with the time of the near-Sun observations
69 to yield an arrival time at Earth.

70 Most arrival time models fall within three categories- empirical models, drag-based
71 models, and MHD models. Empirical models use a relation between observable param-
72 eters and the transit time that is derived from a set of previously observed CMEs and
73 their transit times. This is the simplest type of arrival time model with essentially in-
74 stantaneous computation time. Notable examples include the Effective Acceleration Model
75 (EAM, Paouris & Mavromichalaki, 2017) and the Empirical Shock Arrival or Empirical
76 CME Arrival (ESA and ECA, Gopalswamy et al., 2001). In a similar manner, ma-
77 chine learning techniques can be used to generate simple arrival time models (Liu et al.,
78 2018).

79 Drag-based models use a physics-based equation to calculate the drag between a
80 CME and the background solar wind, which determines the CME velocity as a function
81 of time as well as the arrival time. While more complicated than empirical models, drag-
82 based models still tend to be fairly computationally efficient. These models tend to in-
83 tegrate similar forms of a standard drag equations but the models vary greatly in dimen-
84 sionality and the approaches used to represent the CME structure in a simplified man-
85 ner. Examples include the Drag Based Model (DBM Vršnak et al., 2013), the Enhanced
86 Drag Based Model (Hess & Zhang, 2015), the Ellipse Evolution Model (EIEvo Möstl et
87 al., 2015), a version of EIEvo using data from Heliospheric Imagers (EIEvoHi Rollett et
88 al., 2016), and a probabilistic version of the DMB (P-DBM Napoletano et al., 2018).

89 The last type of model is full MHD models. These models simulate a full background
90 solar wind, then simply embed a CME as either a hydrodynamic or magnetic structure
91 at the inner boundary. The motion is then fully determined by the MHD equations and
92 the CME is not treated distinctly from the background solar wind. These models are the
93 most sophisticated but also the most computationally expensive, making it currently im-
94 practical to use them for ensemble predictions before an actual CME arrival. These mod-
95 els differ in the approaches used for the background solar wind and how the CME is rep-
96 resented and embedded into the simulation. MHD models currently capable of arrival
97 time predictions include SWMF AWSOM (Jin et al., 2017), ENLIL (Odstrcil et al., 2004),
98 EUHFORIA (Pomoell & Poedts, 2018), and SUSANOO (Shiota & Kataoka, 2016).

99 While this process of predicting arrival times appears relatively straightforward,
100 there are some subtleties. First, one should consider whether or not a CME will actu-
101 ally impact the Earth or it will miss it entirely. This is often not directly addressed in
102 arrival time studies, but is a critical aspect of space weather predictions. Second, if a CME
103 travels faster than the speed at which information can propagate through the background
104 solar wind it will drive a shock wave ahead of it. Some arrival time models simulate the
105 arrival of the shock, when present, while others focus on the main body of the CME. Both
106 versions can be useful, but caution must be exercised when comparing with observations
107 or between different models. Finally, most arrival time models require some level of hu-
108 man input, which can lead to different users obtaining different results. This difference
109 from user to user is often only in determining the input parameters. Many morpholog-
110 ical models are based on a visual best fit to observations rather than a deterministic value.
111 In some cases, however, expert operators use the raw output from a deterministic model
112 in combination with additional observations and their experience determine an arrival
113 time (Riley et al., 2018), sometimes referred to as “forecaster-in-the-loop” or “human-
114 in-the-loop”.

115 To better understand the intricacies of predicting CME arrival time the CME Ar-
116 rival Time and Impact Working Team was formed¹ (Verbeke et al., 2019). This work was
117 originally facilitated by NASA’s Community Coordinated Modeling Center (CCMC) and
118 is now a part of the International Space Weather Action Teams (ISWAT). As part of this
119 project, the CCMC maintains the Arrival Time Scoreboard, a web-based system where
120 modelers can submit their predictions for observed events before their actual arrival. As
121 of 2019, the Arrival Time Scoreboard had over 20 registered models, roughly split be-
122 tween predicting the arrival time of the shock or the CME.

123 Verbeke et al. (2019) report on the current progress of the CME Arrival Time and
124 Impact Working Team. The initial focus of the team has been to establish the param-
125 eters of a validation study. They have defined the metadata that should be collected, which
126 will ensure that future model results are reproducible, as well as the metrics that will
127 be used to assess the performance of each model. Finally, they have identified the CMEs
128 that should be simulated and plan to produce a set of input parameters for each CMEs’
129 size, speed, and location. Ensuring that all models are producing results for the same
130 cases with the same inputs will greatly facilitate future comparison studies and better
131 understanding of the difference between the models themselves.

132 Recently, Riley et al. (2018) analyzed the predictions submitted to the CCMC Ar-
133 rival Time scoreboard. This combines results from 32 different models for 139 unique
134 CMEs. Most models have predictions for fewer than 10 CMEs, making it difficult to as-
135 sess their individual capabilities, but five models have predictions for more than 50 CMEs.
136 For all cases, Riley et al. (2018) find an average error of -3.7 hours, indicating a slight
137 bias towards early predictions. The mean absolute error is 12.9 hours and the standard
138 deviation is 17.1 hours, which are better measures for the accuracy of the model as po-
139 sitive and negative errors balance out in an unweighted average. We note that of these
140 32 models, 8 of them use some form of the ENLIL model. Despite using the same core
141 model, these 8 can have very different results, showing the sensitivity to the chosen val-
142 ues of arrival time input parameters. Similarly, Wold et al. (2018) consider 279 CMEs
143 impacting either Earth or one of the STEREO satellites and find an average absolute
144 arrival-time prediction error of 10.4 hours and an unsigned error of -4.0 hours using an
145 ENLIL model.

146 Ensemble modeling can be a useful tool for more thoroughly characterizing arrival
147 time predictions. One performs a set of model runs, or ensemble, each with slight vari-
148 ation in the input parameters, representing the typical range in their uncertainty from
149 observations. Unlike a single instance of a model, the ensemble results give information
150 on the range of possible arrival times, as well as the likelihood of each outcome. Pizzo
151 et al. (2015) lay out much of the theoretical work for using arrival time ensembles for
152 predictions using a version of ENLIL with a highly simplified solar wind background. A
153 coarse-grid run requires about 30 seconds of computational time on a supercomputer so
154 an ensemble of 100 ENLIL simulations would require roughly an hour. While not im-
155 possible for individual studies, this computational requirement may not be sustainable
156 for long-term operations so alternative ensemble models may be preferable, such as the
157 Drag Based Ensemble Model (Dumbović et al., 2018, DBEM), which performs a ensem-
158 ble of DBM models. For 25 CMEs, Dumbović et al. (2018) created ensembles of nearly
159 11,000 runs for each CME and found a mean absolute error of 14.3 hours. This error is
160 comparable to the values found in the previous studies and the simplicity of DBM al-
161 lows for roughly 1000 runs per second on a normal computer. citeAAME18 performed
162 an ensemble of EIEvoHI simulations for the 3 November 2010 CME, which impacted STEREO-
163 B, and study the sensitivity of the transit time to specific input parameters.

¹ Information at <https://ccmc.gsfc.nasa.gov/assessment/topics/helio-cme-arrival.php>

164 In this work we use ensembles to address a specific question- which parameters need
 165 to be known the most accurately to improve arrival time predictions. Using a drag-based
 166 model we perform large parameter space explorations and determine how the arrival time
 167 changes as each input parameter is varied. This information is essential as it will help
 168 focus future research strategies for improving arrival time predictions beyond the cur-
 169 rent mean absolute error of about 10 hours.

170 2 Model and Ensemble Parameters

171 We use ANother Type of Ensemble Arrival Time Results (ANTEATR, Kay & Gopal-
 172 swamy, 2018) to study the sensitivity of drag-based arrival time modeling to various in-
 173 put parameters. ANTEATR was developed to take the output from ForeCAT (Kay et
 174 al., 2015), a model for the coronal deflections and rotations of CMEs due to background
 175 magnetic forces. Figure 1 shows the toroidal CME shape used in both ForeCAT and ANTEATR.
 176 The top of Figure 1 shows side and front views of the gray torus along with the location
 177 of the CME nose and flanks. The torus is assumed to have a circular cross section but
 178 the toroidal axis (maroon dashed line) need not be circular. The toroidal direction points
 179 along the toroidal axis and the poloidal direction points in/out of the page in the side
 180 view. In the front view the poloidal and toroidal directions are shown with a dark blue
 181 and maroon arrows, respectively.

182 The CME shape is defined by the two semi-axis of the toroidal axis (light blue dashed
 183 lines marked a and c) and the cross-sectional width (light blue dashed line marked b).
 184 In practice we define the torus using the angular width $AW = \arctan((b + c)/(R - a -$
 185 $b))$, where R is the radial distance of the CME nose, and two shape ratios $A =$
 186 a/c and $B = b/c$.

We propagate the torus to 1 AU using the standard hydrodynamic drag equation.

$$F_d = C_d A \rho_{SW} (v_{CME} - v_{SW}) |v_{CME} - v_{SW}| \quad (1)$$

187 In Equation 1, the drag force, F_d , is determined from the drag coefficient (C_d), the cross-
 188 sectional area of the CME in the direction of propagation (A), the background solar wind
 189 density (ρ_{SW}), the CME velocity (v_{CME}), and the solar wind velocity (v_{SW}). We will re-
 190 fer to the solar wind density by the number density n_{SW} , which we take to be the mass
 191 density divided by the proton mass. ANTEATR calculates a single force for the entire
 192 CME, which is assumed to propagate as a rigid torus. The net acceleration is determined
 193 by dividing the force by the CME mass, which uniformly decelerates the radial veloc-
 194 ity of the entire CME (or accelerates in the case of CMEs slower than the background
 195 solar wind). This acceleration continually modifies the radial CME velocity as it prop-
 196 agates out, yielding a transit time and radial velocity upon impact. Note throughout this
 197 work we refer to the sensitivity of the arrival time and transit time interchangeably as
 198 the arrival time is simply the transit time added to the CME start time and we do not
 199 consider variations in the start time.

200 In general, the determination of the transit time can be broken down into three fac-
 201 tors. For the purposes of this illustration we assume the CME is faster than the back-
 202 ground solar wind. The first factor we will refer to as the “drag-free nose impact” tran-
 203 sit time, or T_0 . This is the absolute minimum amount of time the CME could take to
 204 propagate to 1 AU, equivalent to the distance traveled divided by the coronal CME ve-
 205 locity. Still ignoring the effects of drag, the transit time will increase as the impact moves
 206 away from the nose toward the flank, giving us the “drag-free actual impact” transit time,
 207 or T'_0 . Finally, the actual transit time, T , will further increase when drag is included and
 208 the CME velocity decreases during the transit.

209 For all models, T_0 will be the same if the same initial distance and velocity are used.
 210 Equation 1 is used by most drag-based models, including the simplification to a one-dimensional

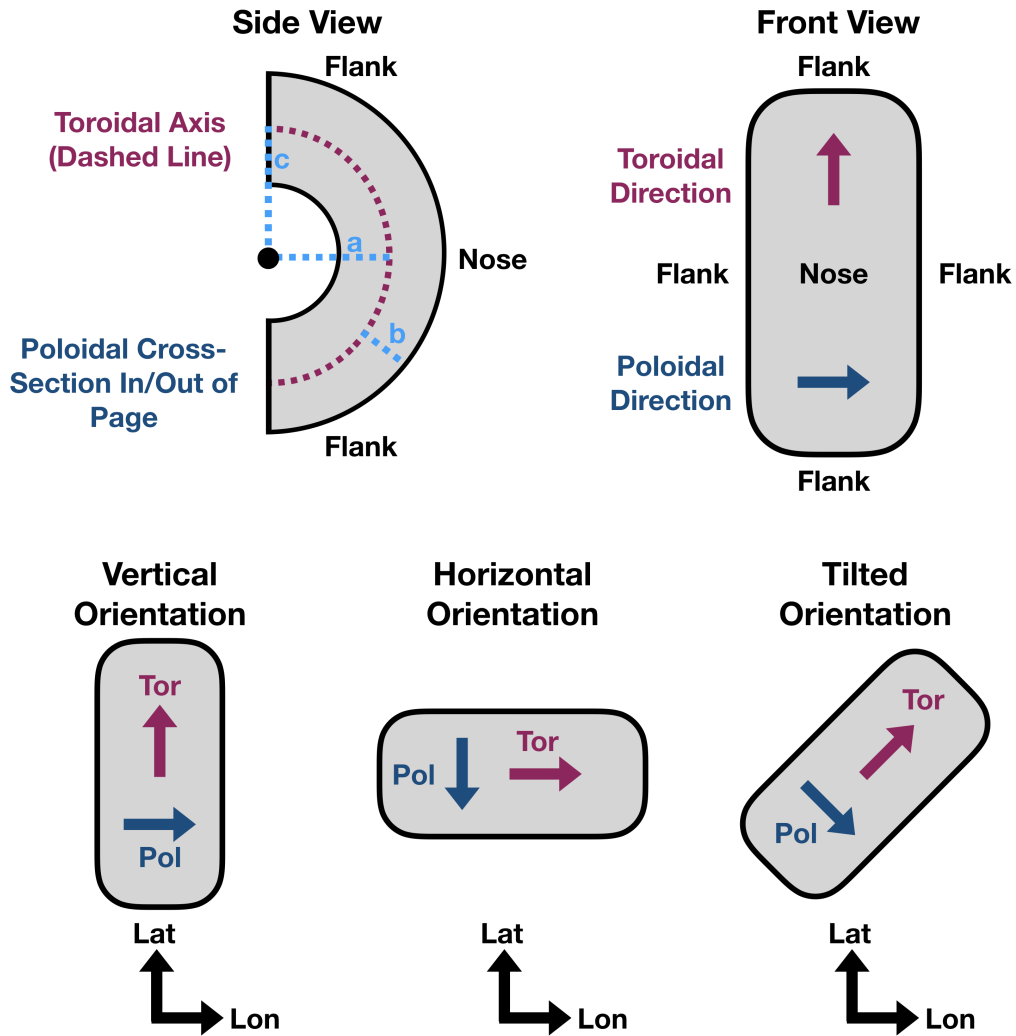


Figure 1. Cartoon showing a side view and a front view of the ANTEATR torus and illustrating the toroidal and poloidal directions (maroon and dark blue, respectively). The bottom illustrates how the toroidal and poloidal directions relate to the latitudinal and longitudinal directions for different CME orientations.

211 drag force. If T'_0 is the same, A is calculated similarly, and the same background solar
 212 wind is used then these models should yield similar T . Models differ the most when it
 213 comes to how the CME shape is approximated, and therefore the location of impact and
 214 the cross-sectional area differ as well, which will affect both T'_0 and T .

215 ANTEATR differs from most drag-based models when it comes to determining the
 216 relative location of the CME and Earth or satellite of interest. We use the full three-dimensional
 217 shape and location to determine when impact first occurs rather than reducing the prob-
 218 lem to one or two dimensions by taking a cut along the CME nose or along the expected
 219 direction of impact. Any uncertainty in this direction due to the inherent projection ef-
 220 fect introduced by coronagraphs will affect the arrival time. In addition to exploring the
 221 sensitivity to parameters explicitly included in the drag equation we will determine the
 222 extent to which the CME position influences the transit time. The simplifications in ge-
 223 ometry introduced by other models could potentially cause errors in the arrival time on
 224 the scale of the variations induced by changes in the CME's three-dimensional position.

225 We wish to determine which parameters are the most critical for determining ac-
 226 curate arrival time predictions. This may vary from CME to CME, particularly for dif-
 227 ferent size or speed CMEs. A CME that initially propagates at nearly the same speed
 228 as the background solar wind will not be affected the same as a CME initially much faster
 229 than the background solar wind. To account for this we consider CMEs of different "strengths"
 230 and create an ensemble for each strength. We use the term strength to refer to a unique
 231 combination of CME mass, speed, and size, with weak CMEs being less massive, slower,
 232 and smaller than strong CMEs. We will refer to different strength CMEs by their kinetic
 233 energy, KE , or the base-10 logarithm of the KE in erg. While this parameter incorpo-
 234 rates the changing velocity and mass at each strength we emphasize that the angular width
 235 is simultaneously increasing.

We consider CMEs between masses of 10^{15} g and 5×10^{16} g. Based on the prop-
 erties of the observed CMEs used in Kay and Gopalswamy (2017), we determine linear
 scalings between the logarithm of the CME mass and the peak radial velocity and angu-
 lar width

$$v = 660 \log_{10} M_{\text{CME}} - 9475 \quad (2)$$

$$AW = 19.8 \log_{10} M_{\text{CME}} - 270 \quad (3)$$

236 where M_{CME} is in g and the resulting v and AW are in km/s and $^\circ$, respectively.
 237 For our range of CME masses this corresponds to velocities between 425 and 1550 km/s
 238 and angular widths between 27 and 61° . These masses and velocities cause our CMEs
 239 having a $\log(\text{KE})$ between 30.0 and 32.8, which ranges from roughly average to an ex-
 240 treme value (e.g. Gopalswamy et al., 2009).

241 Kay and Gopalswamy (2017) used the Graduated Cylindrical Shell stereographic
 242 reconstruction technique (Thernisien et al., 2006) to determine the angular width of the
 243 CMEs. This angular width is not the full angular width rather the angle between the
 244 nose and flank of the CME (half angle). As in Kay and Gopalswamy (2017) we use this
 245 angle to determine the span of our torus shape. In this work we use fixed values of 0.75
 246 and 0.55 for the shape parameters A and B , the average of the cases in Kay and Gopal-
 247 swamy (2017). When determining the sensitivity to the location of impact we use b_{pol}
 248 and b_{tor} , which are the impact parameters in the poloidal and toroidal direction. We de-
 249 fine these as between -100 and 100 with 0 representing the center in that cross-sectional
 250 direction and ± 100 representing the edges. We find that our results are not particularly
 251 sensitive to the precise shape parameter values when we consider changes in terms of the
 252 impact parameters, though they certainly affect the conversion between impact param-
 253 eter and degrees.

254 The ensembles are generated from a seed case by linearly sampling a range about
 255 each input parameter. The seed case for strength CME has a unique mass, velocity, and

Table 1. Seed Values and Ensemble Ranges

Parameter	Seed Value	Range
b_{pol}	0	± 100
b_{tor}	0	± 100
v_{CME}^*	425-1550 km/s	$\pm 50\%$
M_{CME}^*	10^{15} - 5×10^{16} g	$\pm 50\%$
AW^*	27 - 61°	$\pm 50\%$
v_{SW}	440 km/s	$\pm 25\%$
n_{SW}	6.9 cm^{-3}	$\pm 75\%$
C_d	1	$\pm 100\%$

angular width but all other parameters are the same. Table 1 lists the seed values with the “*” indicating a value that scales with CME strength. For each strength ensemble we vary each input parameter individually, running 30 simulations covering the range shown in Table 1. Each strength ensemble contains the seed case and 8 sets of 20 unique simulations and we consider 30 different strengths. Note that for each strength case the range for the velocity, mass, and AW are determined using $\pm 50\%$ of its specific seed values.

Typically when we run ANTEATR we include the orbit of the Earth about the Sun, which causes roughly a degree change in longitude for each day of transit. Here we wish to focus on the change in transit time (Δt) rather than the absolute value and this comparison is easiest when all impacts occur at the CME nose (except for the impact parameter study). To facilitate this we exclude the orbital effects in this work. These secondary effects from small changes in the location of impact due to small changes in the Earth’s orbital location are equivalent changes in the impact parameter of roughly a degree. The results of this work show that this magnitude of changes are negligible when the impact occurs near the CME nose.

3 Ensemble Results

We group our parameters into three sets - parameters related to the CME position, properties of the CME itself, and background solar wind properties. The results for these sets are shown in Figures 2-4, and discussed in Sections 3.1-3.3. For each parameter we first consider the percentage change in the transit time for a percentage change in the parameter. While percentages are not the most intuitive for forecasting, this normalization helps illuminate some of the trends across different strength CMEs. The ranges of the input parameters are not uniform between different parameters as we expect to be able to predict certain parameters more accurately than others. Table 1 shows these ranges. We also show the corresponding change in transit time for a given percentage change in input parameter. Finally, we use the information from each ensemble to derive the hourly change in transit time as a function of input parameter (in natural units) and CME strength.

Figures 2-4 all have the same format. Each row contains the results for an individual input parameter. Within that row the left panel shows percentage change in transit time versus percentage change in input, the middle shows hourly change in transit time versus percentage change in input, and the right shows hourly change in transit time as a function of change in input parameter and CME strength (labeled according to the $\log KE$).

In the left and middle panels, each point is colored according to the CME strength with darker colors representing average CMEs and brighter colors representing extreme

292 CMEs. For each strength we determine the transit time of the control case (unperturbed
 293 initial parameters) and subtract this from each ensemble member to determine the change
 294 in transit time. Positive changes indicate a delay in arrival time (longer transit time) and
 295 negative indicates early arrival. Dashed lines are shown every 10% (left panels) or 5 hours
 296 (middle panels) to illustrate the difference in scales between different parameters.

297 To facilitate comparison between different strength ensembles we fit a natural cubic
 298 spline to each set. The resulting spline is shown by a line matching the color for that
 299 strength CME. Often polynomial and spline fits are subject to the Runge phenomena
 300 where the best fit oscillates wildly near the extreme points. Using a natural spline en-
 301 sures that the fit is well-behaved at near the edges by forcing a linear profile beyond the
 302 extreme points.

303 We use the spline fits to develop a continuous distribution of change in transit time
 304 as a function of change in input parameter and CME strength, which we show as a con-
 305 tour plot in the right panels. While the strength is labeled using the logKE we remind
 306 that this represents a simultaneous change in mass, speed, and angular width. The con-
 307 tours are scaled to saturate at ± 10 hours, the current average absolute uncertainty in
 308 arrival time predictions. Red indicates early arrivals and blue indicates delays. Contour
 309 lines are drawn every two hours in change in arrival time, excluding zero for readabil-
 310 ity. We allow for an extrapolation of 25% beyond the range used to fit the splines, a some-
 311 what arbitrary but reasonable limit to the extent to which we can trust the interpola-
 312 tion. Grey shaded regions indicate values outside this limit, which are likely beyond the
 313 range of uncertainty in the input parameters.

314 3.1 CME Position

315 For the position we consider the impact parameter in either the toroidal or poloidal
 316 directions b_{pol} and b_{tor} . Our ensembles are centered about an impact directly at the CME
 317 nose and our CME is horizontal so that the toroidal axis lies within the ecliptic plane.
 318 Accordingly, changes in latitude and longitude correspond respective to changes in the
 319 poloidal and toroidal directions. If we change the CME orientation we see the same de-
 320 pendence on the the toroidal and poloidal impact parameters, but these now correspond
 321 to different directions in terms of latitude and longitude. The bottom of Figure 1 illus-
 322 trates how different CME orientations lead to the toroidal and poloidal directions cor-
 323 responding to different combinations of the latitudinal and longitudinal directions.

324 Figure 2a shows that moving from the nose ($b_{\text{pol}}=0$) to the extreme poloidal flank
 325 ($b_{\text{pol}}=\pm 100$) causes changes up to 25% in the transit time with the percentage increas-
 326 ing with CME strength. Since the transit time decreases with CME strength we actu-
 327 ally see little variation when the results are expressed in hours. The largest changes cor-
 328 respond to an 8 hour delay, as seen in Figure 2b. The transit time is particular insen-
 329 sitive to the position near the CME nose, any position out to about 60% of the poloidal
 330 width will produce a transit time within 2 hours of the control case. The sensitivity to
 331 precise position rapidly increases as the impact moves towards the flanks, changing by
 332 4 hours for positions in the outer 40% of the poloidal radius.

333 The changes are much larger for the toroidal impact parameter, shown in the bot-
 334 tom row of Figure 2, since our CME shape extends much farther in the toroidal direc-
 335 tion than the poloidal direction. We again find the results are more sensitive near the
 336 flanks than the nose. Looking at variations with CME strength we find that the sensi-
 337 tivity initially increases as we move from the average cases toward the fast CMEs, but
 338 then begins decreasing again as we continue toward the extreme CMEs. The powerful
 339 CMEs are physically larger and therefore have a greater difference between radial dis-
 340 tance of the front at the nose and flank. Their velocity is also faster, however, so it takes
 341 less time to cover a given distance. The turnover occurs when the speed outweighs the
 342 size, and may occur at a different strength if using a different CME shape. The largest

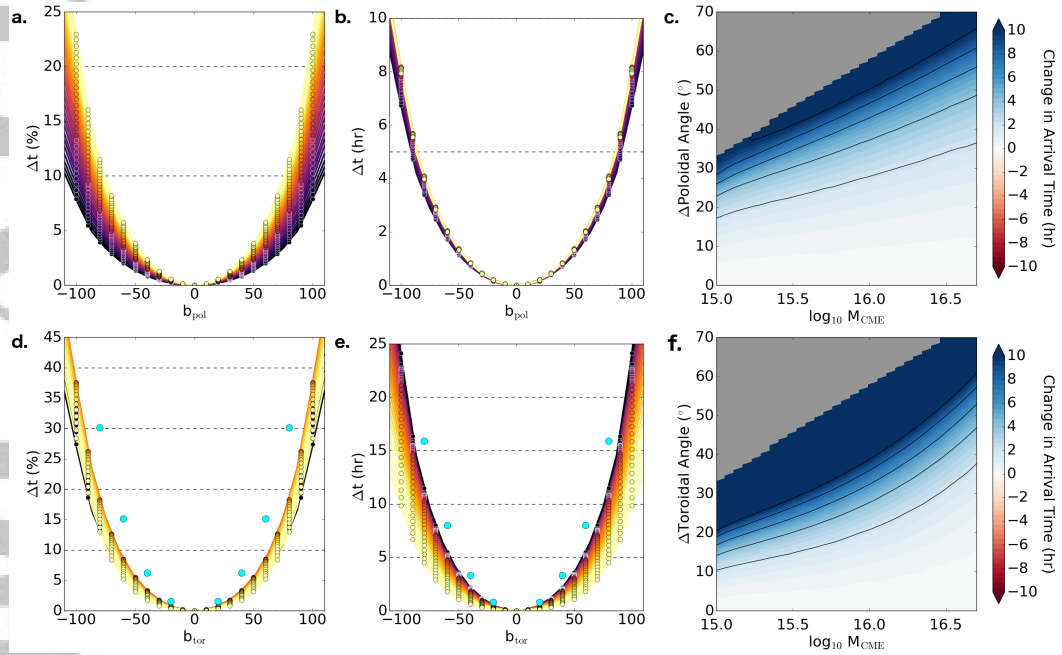


Figure 2. Sensitivity of transit time to positional input parameters. The left column shows the percent change in transit time for a percent change in input parameter. The middle column shows the same in hours. In these panels the different colors indicate different strength CMEs with brighter colors representing more extreme CMEs. The right panel shows contours of change in transit time, in hours, for changes in inputs in natural units (e.g. degrees in this Figure) and different size CMEs, labeled using the CME mass as a proxy. The top row shows results for the poloidal impact parameter and the bottom shows the toroidal impact parameter.

343 delays actually occur for the average CMEs, reaching about 25 hours despite only be-
 344 ing a 27% change but having a long transit time.

345 Figure 2c and 2f show the contours of change in transit time extrapolated from the
 346 spline fits. Little change is observed for all strengths near the nose, only near the flanks
 347 does the transit time begin to change rapidly. For most masses, a change in position of
 348 10° near the flanks can easily produce a 10 hour change in arrival time. Changes cor-
 349 responding to the grey shaded region in Figure 2c and 2f correspond to no impact oc-
 350 ccurring as one has moved beyond the extent of the CME. These factors make the CME
 351 position a very odd parameter when it comes to determining arrival time. For most cases
 352 the results are insensitive but for a small subset the arrival time is extremely sensitive
 353 and it can even lead to uncertainty in whether or not impact actually occurs.

354 Since our control cases impacts at the CME nose, changes in position, either poloidal
 355 or toroidal, can only result in a delay in transit time. Note that for predictions, if the
 356 impact was expected toward the flanks then the uncertainty in position bring the im-
 357 pact closer to the flank or the nose, respectively leading to either a delay or early arrival.

358 3.2 CME Parameters

359 In this section we consider changes in the CME speed, mass, and angular width.
 360 These are the same three parameters that change with our CME strength. Here, the con-
 361 trol cases have the values corresponding to that strength, then an individual parame-
 362 ter is varied while the other two remain constant. All given values of $\log(\text{KE})$ correspond
 363 to the seed values and do not reflect any changes from the parameter space explorations.

364 3.2.1 CME Velocity

365 In the top row of Figure 3 we look at the sensitivity to the CME velocity. Note that
 366 the behavior of Eq. 1 changes when the CME velocity drops below that of the background
 367 solar wind, causing an acceleration instead of a deceleration. All but our weakest con-
 368 trol cases have CME velocities greater than the background solar wind speed, but when
 369 we consider decreases in the CME velocity many ensemble members drop below it.

370 Changes to the CME velocity are the only changes we consider that affect the “drag-
 371 free nose impact” transit time T_0 . An increase in velocity will decrease this time, but
 372 will simultaneously also increase the drag force due to the larger difference from the back-
 373 ground solar wind. The balance between these two effects determines the sensitivity to
 374 the CME velocity.

375 For all but the weakest few cases (below a $\log(\text{KE})$ of 30.6), we see similar behav-
 376 ior for different strength CMEs with a slight increase in sensitivity toward higher strengths.
 377 If we look at changes in terms of hours, these effects again tend to balance out with CMEs
 378 with strengths above a $\log(\text{KE})$ of 30.6 having a delay of 20 hours for a 50% decrease
 379 in CME velocity and an early arrival of 5 hours for a 50% increase in CME velocity.

380 The weakest cases show a rapid change in arrival time for small changes but then
 381 the profiles flatten as the CME velocity approaches and ultimately falls below that of
 382 the background solar wind and the drag begins accelerating the CMEs.

383 Figure 3c shows contours for changes in the CME velocity. The spline plots sug-
 384 gest that and within the range shown in Figure 3c the contours do saturate at ± 10 hours
 385 for all strengths. The transit time is more sensitive to decreases in the CME velocity,
 386 which result in delayed arrival times. For the weakest CMEs, a change of less than 100
 387 km/s causes a 10 hour change in the arrival time. This critical velocity increases with
 388 CME strength with a change of about 600 km/s (300 km/s) corresponding to an early
 389 (late) arrival of 10 hours for a $\log(\text{KE})$ of 31.2 (10^{16} g) CME.

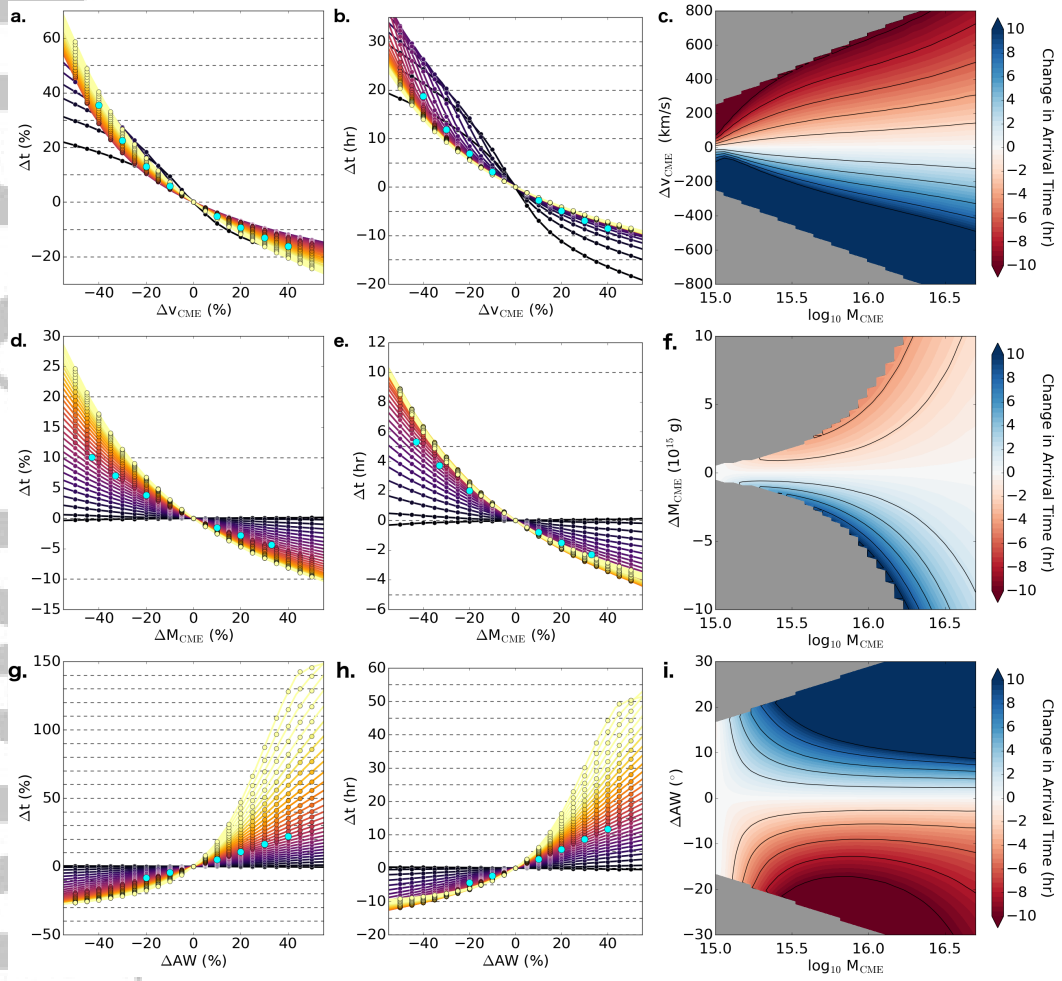


Figure 3. Same as Figure 2 but for the CME velocity (top row), mass (middle), and angular width (bottom).

390 **3.2.2 CME Mass**

391 The middle row Figure 3 shows results for changes in the CME mass. While this
 392 does not factor into the calculation of the drag force, it does determine the extent to which
 393 that force accelerates or decelerates the CME. As expected, as the mass increases the
 394 drag force becomes less effective and the transit time decreases.

395 For the weakest CMEs the velocities are essentially at the solar wind speed so the
 396 drag force is small and changes in the mass have a negligible effect. As the CME strength
 397 increases, so does the drag force and the transit time becomes more sensitive to changes
 398 the CME mass. For the most powerful CMEs a decrease of 50% in the mass corresponds
 399 to a 25% delay and an increase of 50% corresponds to an early arrival by 10%. How-
 400 ever, since these CMEs have the shortest transit times these changes only correspond
 401 to a delay of 9 hours and an early arrival of 4 hours.

402 Figure 3f shows contours of the change in transit time for changes in mass up to
 403 10^{16} g. Increases in mass cause early arrivals of less than 5 hours over the range of pa-
 404 rameters considered. An increase in mass decreases the deceleration from the drag force
 405 so the CMEs gradually approach the drag-free transit time. We find slightly stronger sen-
 406 sitivities to decreases in mass with values approaching a delay of 8 hours at the grey bound-
 407 ary. We note that while we choose not to extrapolate in this region, it already is very
 408 close to the fundamental limit of a 100% decrease in the CME mass. Accordingly, we
 409 suggest that in most cases the CME mass is one of the least essential factors in deter-
 410 mining accurate transit times.

411 **3.2.3 CME Angular Width**

412 The final CME parameter we consider is the angular width, shown in the bottom
 413 row Figure 3, which determines the cross-sectional area of the CME. Changes in the an-
 414 gular width cause the largest variation in transit time with early arrivals up to 30% of
 415 the total transit time for a decrease of 50% in the angular width and delays up to 150%
 416 for a 50% increase. The average CMEs again show little sensitivity due to the weak drag
 417 but we see extreme delays for the most powerful CMEs. These CMEs have the largest
 418 differential speed from the background and in the ANTEATR model the area used in
 419 the drag force is roughly proportional to the square of the tangent of the angular width.
 420 The tangent rapidly increases as the angular width approaches 90° and since the drag
 421 force depends on the square of it it can very effectively decelerate the CME and cause
 422 a large delay of 50 hours if the angular width is underestimated by 30° .

423 In the contours in Figure 3i, we again see that the results are more sensitive to de-
 424 lays (larger angular width) than early arrivals (smaller angular width). Above a $\log(\text{KE})$
 425 of 31.1 an increase of 15° in the angular width causes a delay of 10 hours. In compar-
 426 ison, an early arrival of 10 hours typically requires a change in the angular width greater
 427 than 20° . For the weakest strengths any change in the angular width causes a change
 428 of less than ± 2 hours in the transit time.

429 **3.3 Solar Wind Parameters**

430 The previous parameters were all related to the CME itself but the properties of
 431 the background solar wind may also play an important role in determining the transit
 432 time. For ANTEATR, and similar to many other drag-based models, we use a simple
 433 solar wind that is fully determined by the velocity and number density at 1 AU. In this
 434 section we consider the effects of changes in the solar wind velocity, number density, and
 435 drag coefficient.

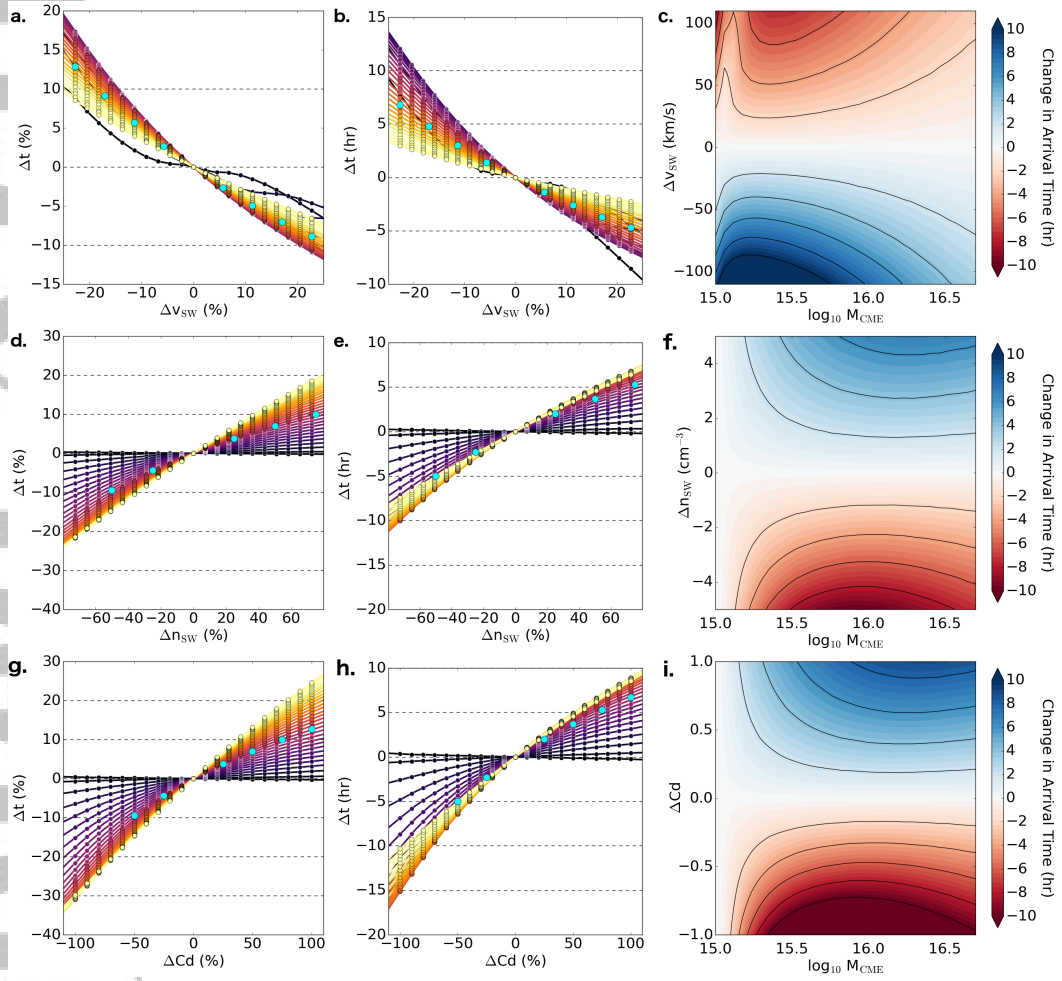


Figure 4. Same as Figure 2 but for the solar wind velocity (top row), number density (middle), and drag coefficient (bottom).

436 **3.3.1 Solar Wind Velocity**

437 The top row of Figure 4 shows that the sensitivity to the solar wind speed tends
 438 to increase as the CME strength decreases. For the average CMEs, where the CME ve-
 439 locity is comparable to the seed solar wind velocity, the trend breaks down as some of
 440 the ensemble members experience accelerations instead of decelerations. We found a sim-
 441 ilar breakdown for the weakest CMEs with the CME velocity in Figure 3a and b. For
 442 a CME with a $\log(\text{KE})$ of 30.6, a decrease of 25% in the background solar wind speed
 443 causes a delay of 12 hours and an increase of 25% in the solar wind speed causes an early
 444 arrival of 7 hours.

445 Figure 4c shows that an accurate background solar wind speed is most critical for
 446 CME strength below a $\log(\text{KE})$ of 30.9. For these smaller CMEs a change of 100 km/s
 447 in the solar wind speed can cause an early arrival up to 8 hours or a delay up to 10 hours.
 448 The white strip in the top left corner of Figure 4c is where the solar wind speed is roughly
 449 equivalent to the CME speed and the sensitivity greatly decreases. The results are not
 450 particularly sensitive for large masses as a change of 100 km/s in the background speed
 451 represents a much smaller fractional change in the differential speed, and therefore less
 452 change to the drag force.

453 **3.3.2 Solar Wind Number Density**

454 The middle row of Figure 4 shows the change in transit time for changes in the so-
 455 lar wind number density. We expect the solar wind density to be less certain than its
 456 velocity so we consider a wider range of percent changes. For a given percentage change,
 457 the results tend to be less sensitive to the solar wind density than the solar wind speed.
 458 As for many parameters, the weakest CMEs show the least sensitivity because they un-
 459 dergo very little deceleration or acceleration since they begin propagation near the back-
 460 ground solar wind speed.

461 The results are less sensitive to the density than for the solar wind velocity with
 462 a change of $\pm 25\%$ only causing changes of ± 2 -3 hours, but a decrease of 75% in the den-
 463 sity causes a early arrival of 10 hours for moderate strength CMEs (around a $\log(\text{KE})$
 464 of 31.3). An increase of 75% causes an delay of 6-7 hours for similar strength CMEs .

465 The most sensitive region shifts towards higher masses for the background solar
 466 wind density, shown in Figure 4f. The majority of parameter space, however, corresponds
 467 to changes less than 6 hours. The largest changes are for a decreases of order 5 cm^{-3}
 468 at a $\log(\text{KE})$ of 31.8, but our background solar wind model has a density of 6.9 cm^{-3}
 469 at 1 AU, so this corresponds to nearly depleting the entire density and a rather extreme
 470 uncertainty in background conditions.

471 A realistic solar wind background would likely have regions of different speeds and
 472 densities along the CMEs path, which is not currently incorporated into our model. This
 473 may suggest that the values found in this section should be considered lower limits on
 474 the uncertainty. If average values are chosen for the speed and density, however, the in-
 475 tegrated effects from over- and under-estimates may average out in terms of the net tran-
 476 sit time. A better understanding of these intricacies would require study beyond the scope
 477 of this paper.

478 **3.3.3 Drag Coefficient**

479 The final parameter we consider is the drag coefficient. ANTEATR and other drag-
 480 based models use the standard form of drag used in hydrodynamics to describe the mo-
 481 tion of a CME through a magnetized background, which was shown to be reasonable by
 482 the simulations of Cargill et al. (1996) and Cargill (2004). The drag coefficient is taken
 483 to be something near unity, similar to hydrodynamics, but this constant incorporates much

484 of the subtleties of the actual physics involved and the precise value is poorly understood.
 485 Kay and Gopalswamy (2018) found optimal arrival times using ANTEATR with a drag
 486 coefficient of 0.8, but only considered six CMEs.

487 Here we assume a control case with $C_d = 1$ and explore values between 0 and 2.
 488 The bottom row of Figure 4 shows these results. As expected, the weakest CMEs are
 489 insensitive to C_d due to their minimal drag. For the strongest CMEs we find that this
 490 causes a decrease of 30% in the transit time or an increase of 25%. The largest early ar-
 491 rivals of 15 hours occurs for a CME mass near a $\log(\text{KE})$ of 31.4 and the strongest CMEs
 492 have a delay of 9 hours.

493 Figure 4i shows the sensitivity to the background drag coefficient. The transit times
 494 are more sensitive to decreases in the drag coefficient. For CMEs with a $\log(\text{KE})$ greater
 495 than about 30.5, the drag free cases (ΔC_d of -1) have transit times differing from the
 496 control by more than 10 hours. An increase of one in the drag coefficient causes delays
 497 of 4-10 hours for similar strength CMEs. It is difficult to address the importance of un-
 498 certainty in the drag coefficient because we do not have a good measure of the actual
 499 range of that uncertainty. If we assume the traditional “near one” means between 0.5
 500 and 1.5 then the uncertainty in the arrival time will be within ± 4 hours. However, the
 501 sensitivity will greatly increase as the range of C_d expands.

502 4 Comparison with Other Models

We have suggested that these sensitivities should be representative for other drag-
 based models and we test this using the DBM model (Vršnak & Žic, 2007), which is avail-
 able for runs on demand in an online web application². The online tool allows for some
 specification of CME and background parameters but differs slightly from ANTEATR
 in the input parameters. The DBM drag acceleration is calculated the same as in ANTEATR
 but the drag coefficient C_d , CME area, solar wind density, and CME mass are combined
 into a single drag parameter Γ .

$$\Gamma = C_d \frac{A \rho_{\text{SW}}}{M_{\text{SW}}} 10^7 \text{km}^{-1} \quad (4)$$

503 The DBM default Γ of $2 \times 10^{-8} \text{km}^{-1}$ is comparable to an ANTEATR CME of 5×10^{15}
 504 g ($\log(\text{KE})$ of 31.3 and near the orange/purple transition in our color scheme and where
 505 the circle outlines switch from black to white in the spline plots). The comparison is not
 506 exact though as the CME shapes are prescribed differently with ANTEATR using a torus
 507 as compared to the DBM’s cone shape with a rounded front. Where possible, we run DBM
 508 simulations using the equivalent changes in input parameters and show the results in Fig-
 509 ures 2-4 with light blue circles. The DBM application restricts Γ to a minimum value
 510 of 0.1, which limits the range of our comparison in some cases. Note that while these fig-
 511 ures show the similarity between the models in the change in transit time, the actual tran-
 512 sit times for the control cases differ by about 6 hours between ANTEATR and DBM.
 513 We emphasize this comparison between models is only for the sensitivities to input pa-
 514 rameters not the actual transit time values.

515 For the CME velocity (Figure 3a-b), mass (Figure 3d-e), angular width (Figure 3g-
 516 h), solar wind density (Figure 4(a-b)), and drag coefficient (Figure 4g-h), the DBM points
 517 fall directly on the equivalent ANTEATR results (orange/purple transition). Since the
 518 models use the same form of the drag equation, they scale similarly with input param-
 519 eters.

² <http://oh.geof.unizg.hr/DBM/dbm.php>

520 For the CME position we take the change in position along the toroidal axis to be
 521 more comparable to the changes for the DBM's axial symmetric shape. Figure 2d-e show
 522 the results for the change in position. We find that the results are similar, but the DBM
 523 tends to be slightly more sensitive, tending to exceed the ANTEATR sensitivity by about
 524 5% or about 2 hours. This results from our toroidal direction having slightly flatter cur-
 525 vature than the DBM shape. We note that we get better agreement for the angular width
 526 than the position because we assume that the area and therefore Γ scales the same as
 527 the ANTEATR area.

528 We also find that ANTEATR is just slightly more sensitive to the background so-
 529 lar wind speed. For the DBM background model the solar wind velocity and density are
 530 intrinsically coupled by assuming a constant mass flux. The solar wind velocity is the
 531 only parameter that can explicitly be modified, not the density or mass flux so we ac-
 532 count for changes in the density in Figure 4a-b by adjusting Γ . An increase in the DBM
 533 solar wind velocity causes a decrease in the density, which will decrease the transit time,
 534 nullifying some of the increase from the velocity increase. We emphasize that the dif-
 535 ference in sensitivity between the two models is small, a decrease of 20% in the veloc-
 536 ity corresponds to less than an hour difference between the delays of ANTEATR and DBM.

537 Finally, we comment on different combinations of variables used by other drag mod-
 538 els, in particular, the sensitivity to Γ . Looking at Equation 4, we find that we have es-
 539 sentially already explore the sensitivity to each of the individual components that factor
 540 into it. Changing either n_{SW} or C_d by a certain percentage is the same as changing
 541 Γ by that same percentage. Looking at Figure 4d and g, a change of -50% in either n_{SW}
 542 or C_d causes a 10% decrease in the transit time for the $\log(\text{KE})$ of 31.3 and the DBM
 543 results. This corresponds to a change of 10^{-8} km^{-1} in Γ . The same information can be
 544 inferred from the mass or angular width, only with marginally more complicated math.
 545 Figure 4i can be most easily used to understand the expected sensitivity to Γ by sim-
 546 ply multiplying the y-axis values by $2 \times 10^{-8} \text{ km}^{-1}$.

547 5 Discussion

548 We wish to use the information from the previous sections to develop suggestions
 549 on where the community should focus its efforts to improve arrival time predictions. We
 550 wish to find the accuracy with which parameters would need to be known for an accu-
 551 racy of 5 hours. While this is a somewhat arbitrary value, it represents a factor of two
 552 improvement in from the current mean absolute error. Table 2 shows these values for
 553 each parameter. For each size CME the top row represents values that lead to an 5 hour
 554 early arrival and the bottom row represents values that lead to a 5 hours delay. A dash
 555 indicates that no values within the range we consider can produce a 5 hour change - that
 556 the transit time is not particularly sensitive to these parameters. We include values for
 557 Γ as well by scaling it from the results for C_d .

558 For an average CME ($\log(\text{KE})$ 30.0, mass 10^{15} g , speed 425 km/s, half-width 27°),
 559 we find the most critical parameter is the CME velocity, requiring an accuracy around
 560 30 km/s or less. The solar wind velocity is also important, as can be the CME position
 561 if the impact is located near the flanks.

562 On the other hand, an extreme CME depends ($\log(\text{KE})$ 32.8, mass $5 \times 10^{16} \text{ g}$, speed
 563 1550 km/s, half-width 60°) most strongly on the angular width, requiring an accuracy
 564 of $5\text{-}10^\circ$. Our extreme corresponds to a very large CME with a kinetic energy only a fac-
 565 tor of 2.5 smaller than that estimated for the Carrington event (e.g. Riley, 2012; Cliver
 566 & Dietrich, 2013). We do not expect such an extreme event to occur as frequently as the
 567 average and fast cases. However, when an extreme CME does occur an accurate mea-
 568 surement of the angular width is absolutely necessary. This will require coronagraph ob-
 569 servations at a viewing angle off the Sun-Earth line, such as L4 or L5. We see that these

Table 2. Minimum Accuracy Needed for 5 Hour Arrival Time Accuracy

CME Size	Pol. Pos. ($^{\circ}$)	Tor. Pos. ($^{\circ}$)	v_{CME} (km/s)	M_{CME} (10^{15} g)	AW ($^{\circ}$)	v_{SW} (km/s)	n_{SW} (cm^{-3})	C_d	Γ (10^{-8}km^{-1})
Average	24.5	15.6	29	–	–	64	–	–	–
	8.0	3.5	-36	–	–	-80	–	–	–
Fast	41.5	31.5	275	7.7	-7.3	110	-2.8	-0.40	-0.8
	13.5	7.5	-198	-3.8	6.0	-80	3.6	0.52	1.04
Extreme	53.0	50.0	400	–	-9.0	–	-3.4	-0.49	-0.98
	14.0	10.5	-283	–	5.0	–	3.8	0.55	1.10

570 extreme events will also be sensitive to the CME velocity, solar wind density, and drag
571 coefficient. In the case of flank encounters the position is again important.

572 We would expect to see CMEs comparable to the fast CME more frequently than
573 the extreme case, particularly during high solar activity. Unfortunately, the accurate de-
574 termination of the transit time of these CMEs seems to combine all the difficulties seen
575 for the slower, average CMEs and more rare, extreme CMEs. Each of the parameters
576 considered in this work can produce a 5 hour change in arrival time. Our instinct is that
577 the angular width will likely be the limiting parameter for these CMEs as an accuracy
578 below 7.5° should require stereoscopic measurements. These are the only CMEs for which
579 the actual CME mass is a limiting factor, but we find that the required accuracy is roughly
580 the same magnitude as the actual CME mass and reconstruction techniques tend to re-
581 produce the mass within a factor of two (Vourlidas et al., 2010). Accurate estimations
582 of the mass of Earth-directed CMEs again require a coronagraph with the Sun-Earth line
583 near the plane of the sky, though recent work shows promise in determining CME mass
584 from EUV dimming (Mason et al., 2016; Dissauer et al., 2019; López et al., 2019).

585 For the position, we show the change in the location of impact along either the poloidal
586 or toroidal direction that would be required to cause a 5 hour delay in the arrival time.
587 For each mass CME the top number is the critical value near the nose and the bottom
588 is the critical value near the flank. For all masses and both toroidal and poloidal direc-
589 tions the results are much more sensitive near the flanks. The critical value near the nose
590 tends to be 3-4 times larger than that near the flank. Both Mays et al. (2015) and Möstl
591 et al. (2015) study the 2014 January 7 CME, a large CME that erupted near disk center
592 and was expected to cause a large geomagnetic storm at Earth but ended up arriv-
593 ing 13 hours later and much weaker than expected. In hindsight, this CME was found
594 to deflect away from disk center, moving the impact toward the flanks. This case study
595 shows that, while not typically the largest source of error, the direction of propagation
596 can certainly be important in individual events.

597 Pizzo et al. (2015) find similar behavior for ENLIL arrival time simulations. Weak
598 to moderate CMEs tend to be the most sensitive to the CME velocity whereas stronger
599 CMEs are most sensitive to the angular width. Pizzo et al. (2015) also found that the
600 sensitivity to CME parameters increased as the impact move away from the nose and
601 toward the flanks, something we have not considered in this work. As such, we expect
602 that the numbers in Table 2 could represent lower limits to the critical values needed for
603 5 hour accuracy.

604 Finally, we emphasize that the entirety of this work has considered the effects of
605 varying a single parameter at a time. While this is useful for identifying the key param-
606 eters to focus on for immediate improvement in predictions, further study must be done
607 to understand how uncertainty in multiple parameters compounds. In this work we have

608 scratched the surface showing how the sensitivity changes for different “strength” CMEs,
609 but this is only a first step as we assume uniform scaling of mass, speed, and size.

610 **6 Conclusion**

611 We have used the simple arrival time model ANTEATR to better understand how
612 arrival time changes with various input parameters. We select a range representative of
613 our current observational uncertainty in each input parameter and determine the cor-
614 responding range in arrival times. This information allows us identify to identify the most
615 critical parameters for accurate arrival time predictions.

616 We produce results for CMEs of different “strengths,” simultaneously varying the
617 CME size, speed, and mass. For an average CME, we find the CME velocity is the most
618 important parameter whereas the angular width is most important for an extreme event.
619 The transit time of a more common fast CME is affected by both the angular width, and
620 to a lesser extent, the CME velocity. The CME position can have a strong influence on
621 the transit time for all strength CMEs when impact occurs near the flanks. The posi-
622 tion can also influence whether or not impact is expected to occur.

623 The background solar wind model is marginally important for all strength CMEs
624 with the solar wind velocity tending to be more important for weaker CMEs and the so-
625 lar wind density more important for faster CMEs. The effects from these solar wind pa-
626 rameters, however, tends not to be as large as those from the CME properties.

627 We compared the ANTEATR results with those from another drag based model
628 and find excellent agreement between the two. The actual transit time differs by a sev-
629 eral hours between the two models but the sensitivity to input parameters is nearly iden-
630 tical. The largest difference in sensitivity is for changes in CME position, which results
631 from slight differences in the CME shape between models. This suggests that the sen-
632 sitivities derived in this work can be reliably extended to other drag-based arrival time
633 models.

634 **Acknowledgments**

635 CK is supported by the National Aeronautics and Space Administration under Grant
636 80NSSC19K0909 issued through the Heliophysics Early Career Investigators Program.
637 CV is funded by the Research Foundation - Flanders, FWO SB PhD fellowship 11ZZ216N.
638 The ANTEATR model and the code used to generate the ensembles are available at [github](https://github.com/ckay314/ANTEATR/releases/tag/v1.0)
639 [.com/ckay314/ANTEATR/releases/tag/v1.0](https://github.com/ckay314/ANTEATR/releases/tag/v1.0) and are archived through Zenodo as [doi:10.5281/zenodo.3533363](https://doi.org/10.5281/zenodo.3533363).

640 **References**

- 641 Amerstorfer, T., Möstl, C., Hess, P., Temmer, M., Mays, M. L., Reiss, M. A., ...
642 Bourdin, P. A. (2018, Jul). Ensemble Prediction of a Halo Coronal Mass
643 Ejection Using Heliospheric Imagers. *Space Weather*, *16*(7), 784-801. doi:
644 10.1029/2017SW001786
- 645 Cargill, P. J. (2004, May). On the Aerodynamic Drag Force Acting on Interplan-
646 etary Coronal Mass Ejections. *Solar Physics*, *221*, 135-149. doi: 10.1023/B:
647 SOLA.0000033366.10725.a2
- 648 Cargill, P. J., Chen, J., Spicer, D. S., & Zalesak, S. T. (1996, March). Magne-
649 tohydrodynamic simulations of the motion of magnetic flux tubes through a
650 magnetized plasma. *Journal of Geophysical Research*, *101*, 4855-4870. doi:
651 10.1029/95JA03769
- 652 Cliver, E. W., & Dietrich, W. F. (2013, Oct). The 1859 space weather event revis-
653 ited: limits of extreme activity. *Journal of Space Weather and Space Climate*,
654 *3*, A31. doi: 10.1051/swsc/2013053

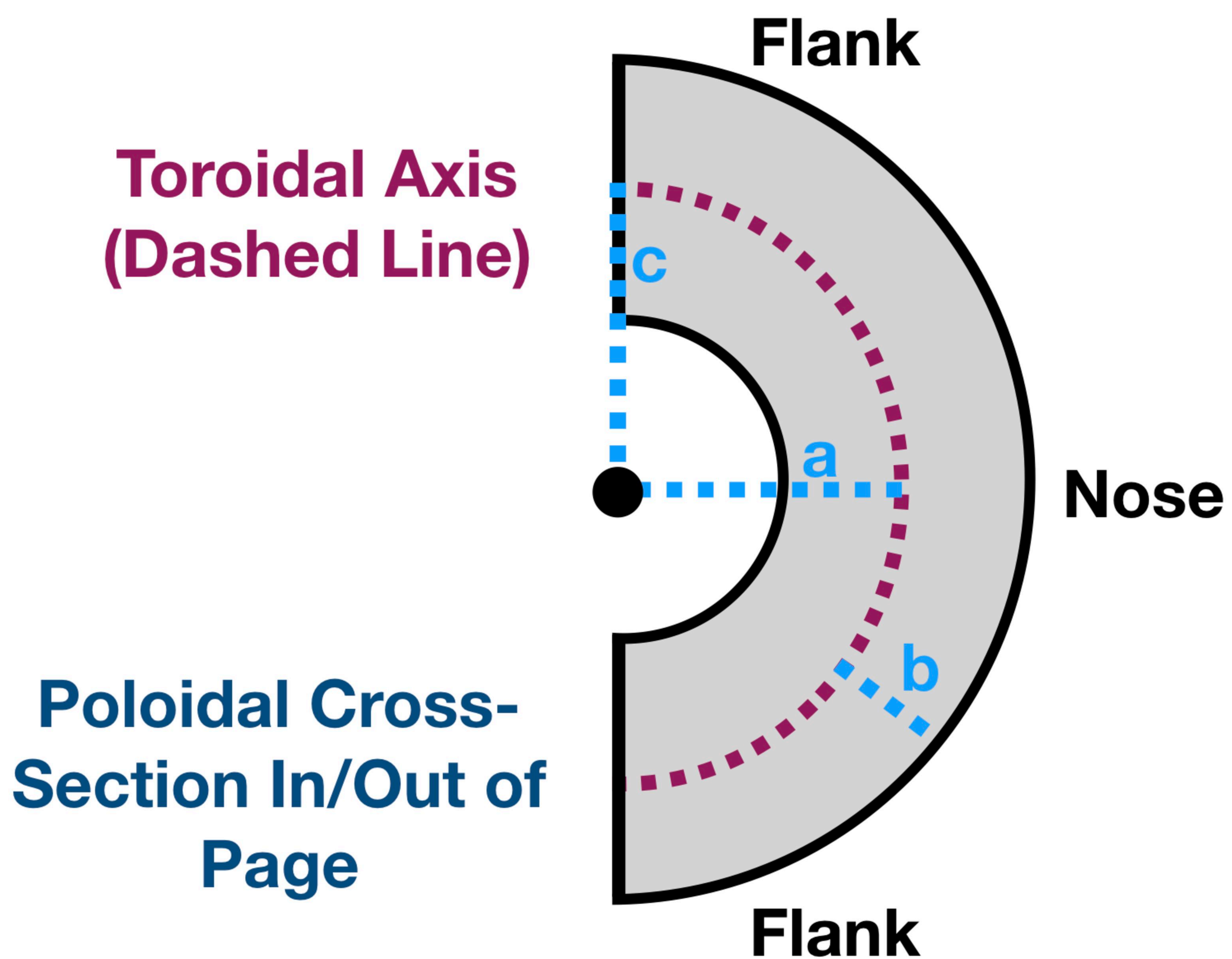
- 655 Dissauer, K., Veronig, A. M., Temmer, M., & Podladchikova, T. (2019, Apr). Statistics of Coronal Dimmings Associated with Coronal Mass Ejections. II. Relationship between Coronal Dimmings and Their Associated CMEs. *The Astrophysical Journal*, *874*(2), 123. doi: 10.3847/1538-4357/ab0962
- 656
657
658
- 659 Dumbović, M., Čalogović, J., Vršnak, B., Temmer, M., Mays, M. L., Veronig, A., & Piantšitsch, I. (2018, February). The Drag-based Ensemble Model (DBEM) for Coronal Mass Ejection Propagation. *The Astrophysical Journal*, *854*, 180. doi: 10.3847/1538-4357/aaaa66
- 660
661
662
- 663 Gopalswamy, N., Lara, A., Yashiro, S., Kaiser, M. L., & Howard, R. A. (2001, December). Predicting the 1-AU arrival times of coronal mass ejections. *Journal of Geophysical Research*, *106*, 29207-29218. doi: 10.1029/2001JA000177
- 664
665
- 666 Gopalswamy, N., Yashiro, S., Michalek, G., Stenborg, G., Vourlidas, A., Freeland, S., & Howard, R. (2009, April). The SOHO/LASCO CME Catalog. *Earth Moon and Planets*, *104*, 295-313. doi: 10.1007/s11038-008-9282-7
- 667
668
- 669 Hess, P., & Zhang, J. (2015, October). Predicting CME Ejecta and Sheath Front Arrival at L1 with a Data-constrained Physical Model. *The Astrophysical Journal*, *812*, 144. doi: 10.1088/0004-637X/812/2/144
- 670
671
- 672 Jin, M., Manchester, W. B., van der Holst, B., Sokolov, I., Tóth, G., Vourlidas, A., ... Gombosi, T. I. (2017, January). Chromosphere to 1 AU Simulation of the 2011 March 7th Event: A Comprehensive Study of Coronal Mass Ejection Propagation. *The Astrophysical Journal*, *834*, 172. doi: 10.3847/1538-4357/834/2/172
- 673
674
675
676
- 677 Kay, C., & Gopalswamy, N. (2017, December). Using the Coronal Evolution to Successfully Forward Model CMEs' In Situ Magnetic Profiles. *Journal of Geophysical Research (Space Physics)*, *122*(A11), 11. doi: 10.1002/2017JA024541
- 678
679
- 680 Kay, C., & Gopalswamy, N. (2018, Sep). The Effects of Uncertainty in Initial CME Input Parameters on Deflection, Rotation, B_z , and Arrival Time Predictions. *Journal of Geophysical Research (Space Physics)*, *123*(9), 7220-7240. doi: 10.1029/2018JA025780
- 681
682
683
- 684 Kay, C., Opher, M., & Evans, R. M. (2015, June). Global Trends of CME Deflections Based on CME and Solar Parameters. *The Astrophysical Journal*, *805*, 168. doi: 10.1088/0004-637X/805/2/168
- 685
686
- 687 Liu, J., Ye, Y., Shen, C., Wang, Y., & Erdélyi, R. (2018, March). A New Tool for CME Arrival Time Prediction using Machine Learning Algorithms: CAT-PUMA. *The Astrophysical Journal*, *855*, 109. doi: 10.3847/1538-4357/aaae69
- 688
689
- 690 López, F. M., Cremades, H., Balmaceda, L. A., Nuevo, F. A., & Vásquez, A. M. (2019, Jul). Estimating the mass of CMEs from the analysis of EUV dimmings. *Astronomy & Astrophysics*, *627*, A8. doi: 10.1051/0004-6361/201834163
- 691
692
693
- 694 Mason, J. P., Woods, T. N., Webb, D. F., Thompson, B. J., Colaninno, R. C., & Vourlidas, A. (2016, Oct). Relationship of EUV Irradiance Coronal Dimming Slope and Depth to Coronal Mass Ejection Speed and Mass. *The Astrophysical Journal*, *830*(1), 20. doi: 10.3847/0004-637X/830/1/20
- 695
696
697
- 698 Mays, M. L., Thompson, B. J., Jian, L. K., Colaninno, R. C., Odstrcil, D., Möstl, C., ... Zheng, Y. (2015, October). Propagation of the 7 January 2014 CME and Resulting Geomagnetic Non-event. *The Astrophysical Journal*, *812*, 145. doi: 10.1088/0004-637X/812/2/145
- 699
700
701
- 702 Möstl, C., Rollett, T., Frahm, R. A., Liu, Y. D., Long, D. M., Colaninno, R. C., ... Vršnak, B. (2015, May). Strong coronal channelling and interplanetary evolution of a solar storm up to Earth and Mars. *Nature Communications*, *6*, 7135. doi: 10.1038/ncomms8135
- 703
704
705
- 706 Napoletano, G., Forte, R., Moro, D. D., Pietropaolo, E., Giovannelli, L., & Berrilli, F. (2018, Feb). A probabilistic approach to the drag-based model. *Journal of Space Weather and Space Climate*, *8*, A11. doi: 10.1051/swsc/2018003
- 707
708
- 709 Odstrčil, D., Pizzo, V. J., Linker, J. A., Riley, P., Lionello, R., & Mikic, Z. (2004,

- 710 Oct). Initial coupling of coronal and heliospheric numerical magnetohydrodynamic codes. *Journal of Atmospheric and Solar-Terrestrial Physics*, 66(15-16),
 711 1311-1320. doi: 10.1016/j.jastp.2004.04.007
- 712 Paouris, E., & Mavromichalaki, H. (2017, December). Effective Acceleration Model
 713 for the Arrival Time of Interplanetary Shocks driven by Coronal Mass Ejections.
 714 *Solar Physics*, 292, 180. doi: 10.1007/s11207-017-1212-2
- 715 Pizzo, V. J., de Koning, C., Cash, M., Millward, G., Biesecker, D. A., Puga, L.,
 716 ... Odstrcil, D. (2015). Theoretical basis for operational ensemble forecasting
 717 of coronal mass ejections. *Space Weather*, 13(10), 676-697. Retrieved
 718 from [https://agupubs.onlinelibrary.wiley.com/doi/abs/10.1002/](https://agupubs.onlinelibrary.wiley.com/doi/abs/10.1002/2015SW001221)
 719 [2015SW001221](https://agupubs.onlinelibrary.wiley.com/doi/abs/10.1002/2015SW001221) doi: 10.1002/2015SW001221
- 720 Pomoell, J., & Poedts, S. (2018, Jun). EUHFORIA: European heliospheric forecasting
 721 information asset. *Journal of Space Weather and Space Climate*, 8, A35.
 722 doi: 10.1051/swsc/2018020
- 723 Riley, P. (2012). On the probability of occurrence of extreme space weather events.
 724 *Space Weather*, 10(2). Retrieved from [https://agupubs.onlinelibrary](https://agupubs.onlinelibrary.wiley.com/doi/abs/10.1029/2011SW000734)
 725 [.wiley.com/doi/abs/10.1029/2011SW000734](https://agupubs.onlinelibrary.wiley.com/doi/abs/10.1029/2011SW000734) doi: 10.1029/2011SW000734
- 726 Riley, P., Mays, M. L., Andries, J., Amerstorfer, T., Biesecker, D., Delouille, V., ...
 727 Zhao, X. (2018, Sep). Forecasting the Arrival Time of Coronal Mass Ejections:
 728 Analysis of the CCMC CME Scoreboard. *Space Weather*, 16(9), 1245-1260.
 729 doi: 10.1029/2018SW001962
- 730 Rollett, T., Möstl, C., Isavnin, A., Davies, J. A., Kubicka, M., Amerstorfer,
 731 U. V., & Harrison, R. A. (2016, Jun). ELEvoHI: A Novel CME Prediction
 732 Tool for Heliospheric Imaging Combining an Elliptical Front with
 733 Drag-based Model Fitting. *The Astrophysical Journal*, 824(2), 131. doi:
 734 [10.3847/0004-637X/824/2/131](https://doi.org/10.3847/0004-637X/824/2/131)
- 735 Shiota, D., & Kataoka, R. (2016, February). Magnetohydrodynamic simulation
 736 of interplanetary propagation of multiple coronal mass ejections with inter-
 737 nal magnetic flux rope (SUSANOO-CME). *Space Weather*, 14, 56-75. doi:
 738 [10.1002/2015SW001308](https://doi.org/10.1002/2015SW001308)
- 739 Thernisien, A. F. R., Howard, R. A., & Vourlidas, A. (2006, November). Modeling of
 740 Flux Rope Coronal Mass Ejections. *The Astrophysical Journal*, 652, 763-773.
 741 doi: 10.1086/508254
- 742 Verbeke, C., Mays, M. L., Temmer, M., Bingham, S., Steenburgh, R., Dumbović, M.,
 743 ... Andries, J. (2019, Jan). Benchmarking CME Arrival Time and Impact:
 744 Progress on Metadata, Metrics, and Events. *Space Weather*, 17(1), 6-26. doi:
 745 [10.1029/2018SW002046](https://doi.org/10.1029/2018SW002046)
- 746 Vourlidas, A., Howard, R. A., Esfandiari, E., Patsourakos, S., Yashiro, S., &
 747 Michalek, G. (2010, October). Comprehensive Analysis of Coronal Mass
 748 Ejection Mass and Energy Properties Over a Full Solar Cycle. *The Astrophysical*
 749 *Journal*, 722, 1522-1538. doi: 10.1088/0004-637X/722/2/1522
- 750 Vršnak, B., & Žic, T. (2007, September). Transit times of interplanetary coronal
 751 mass ejections and the solar wind speed. *Astronomy and Astrophysics*, 472,
 752 937-943. doi: 10.1051/0004-6361:20077499
- 753 Vršnak, B., Žic, T., Vrbanec, D., Temmer, M., Rollett, T., Möstl, C., ... Shan-
 754 mugaraju, A. (2013, July). Propagation of Interplanetary Coronal Mass
 755 Ejections: The Drag-Based Model. *Solar Physics*, 285, 295-315. doi:
 756 [10.1007/s11207-012-0035-4](https://doi.org/10.1007/s11207-012-0035-4)
- 757 Wold, A. M., Mays, M. L., Taktakishvili, A., Jian, L. K., Odstrcil, D., & MacNeice,
 758 P. (2018, March). Verification of real-time WSA-ENLIL+Cone simulations of
 759 CME arrival-time at the CCMC from 2010 to 2016. *Journal of Space Weather*
 760 *and Space Climate*, 8(27), A17. doi: 10.1051/swsc/2018005
- 761 Xie, H., Ofman, L., & Lawrence, G. (2004, March). Cone model for halo CMEs: Ap-
 762 plication to space weather forecasting. *Journal of Geophysical Research (Space*
 763 *Physics)*, 109, 3109. doi: 10.1029/2003JA010226

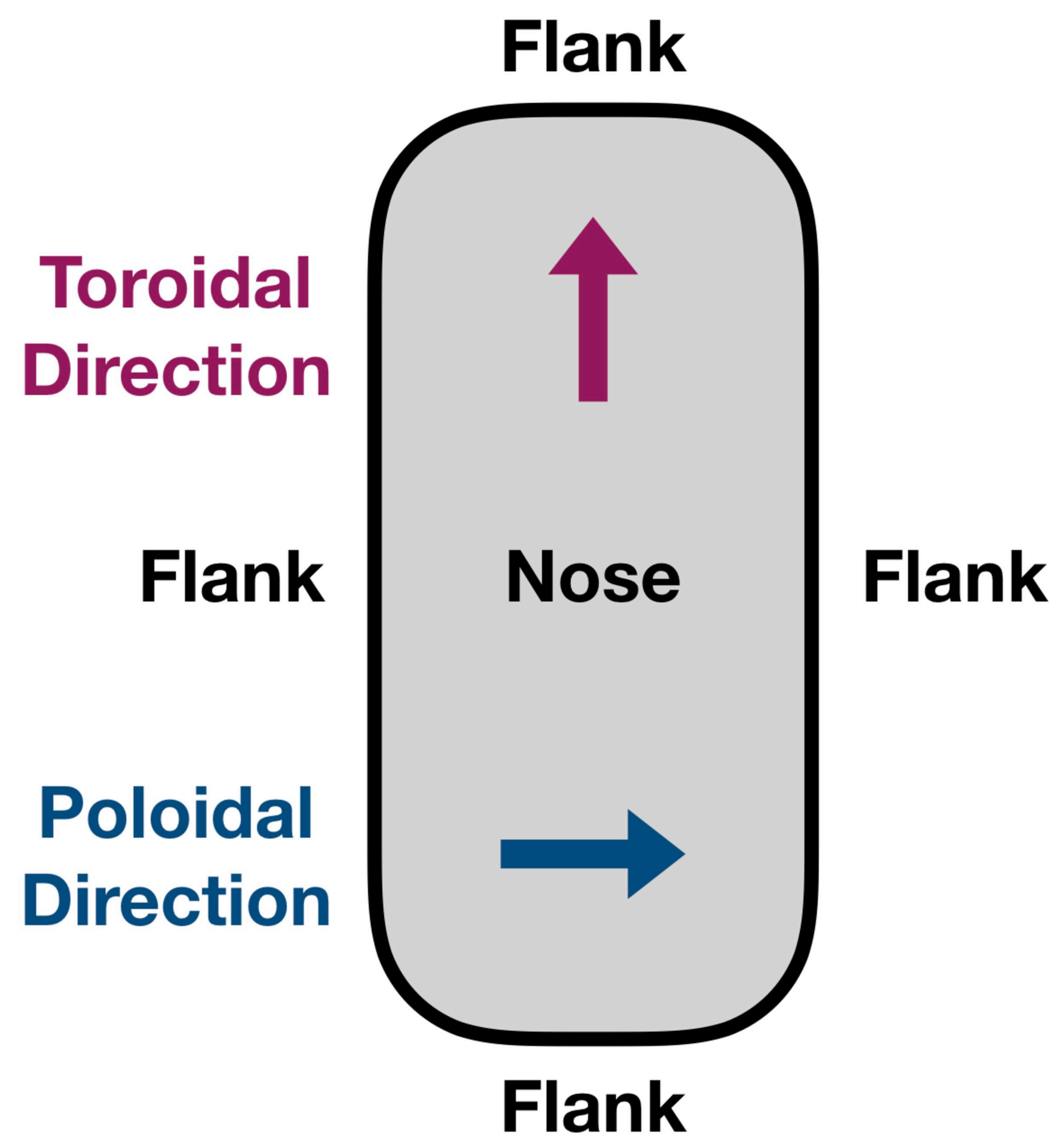
Figure 1.

Accepted Article

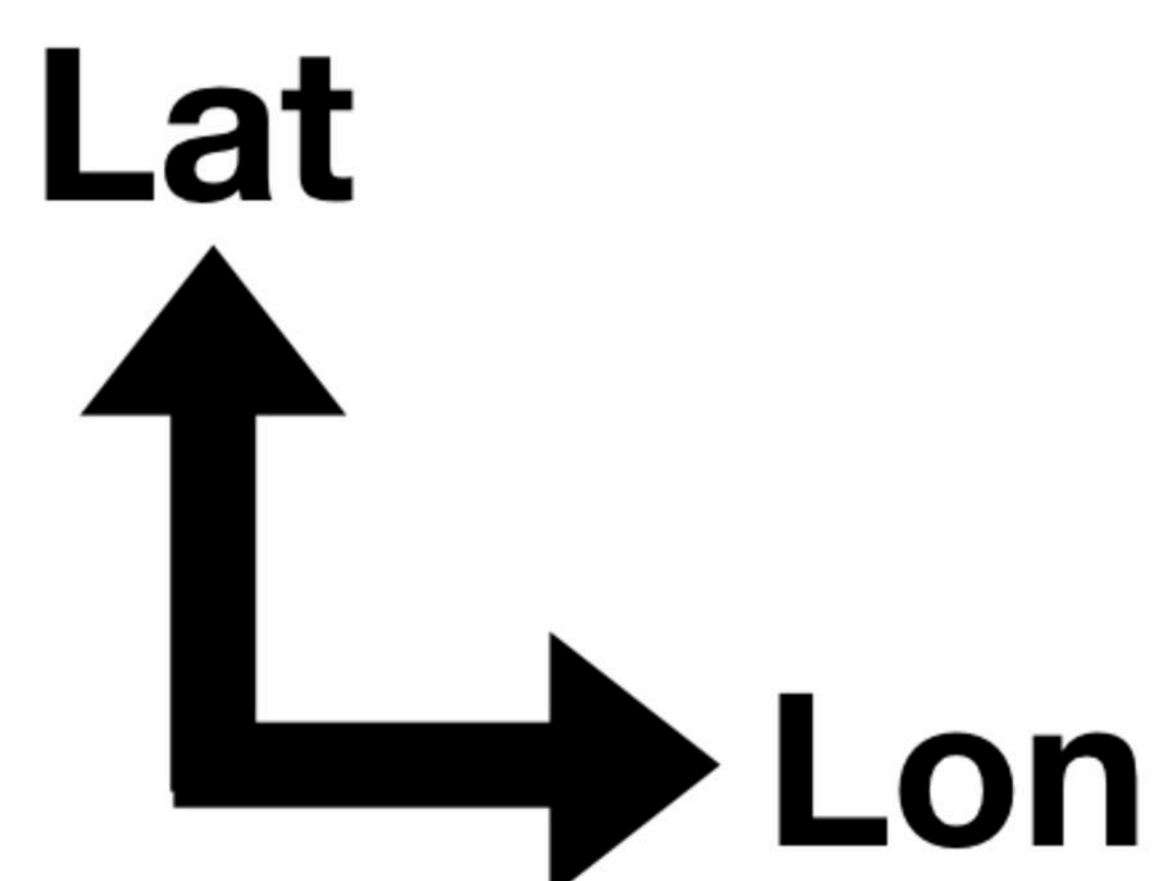
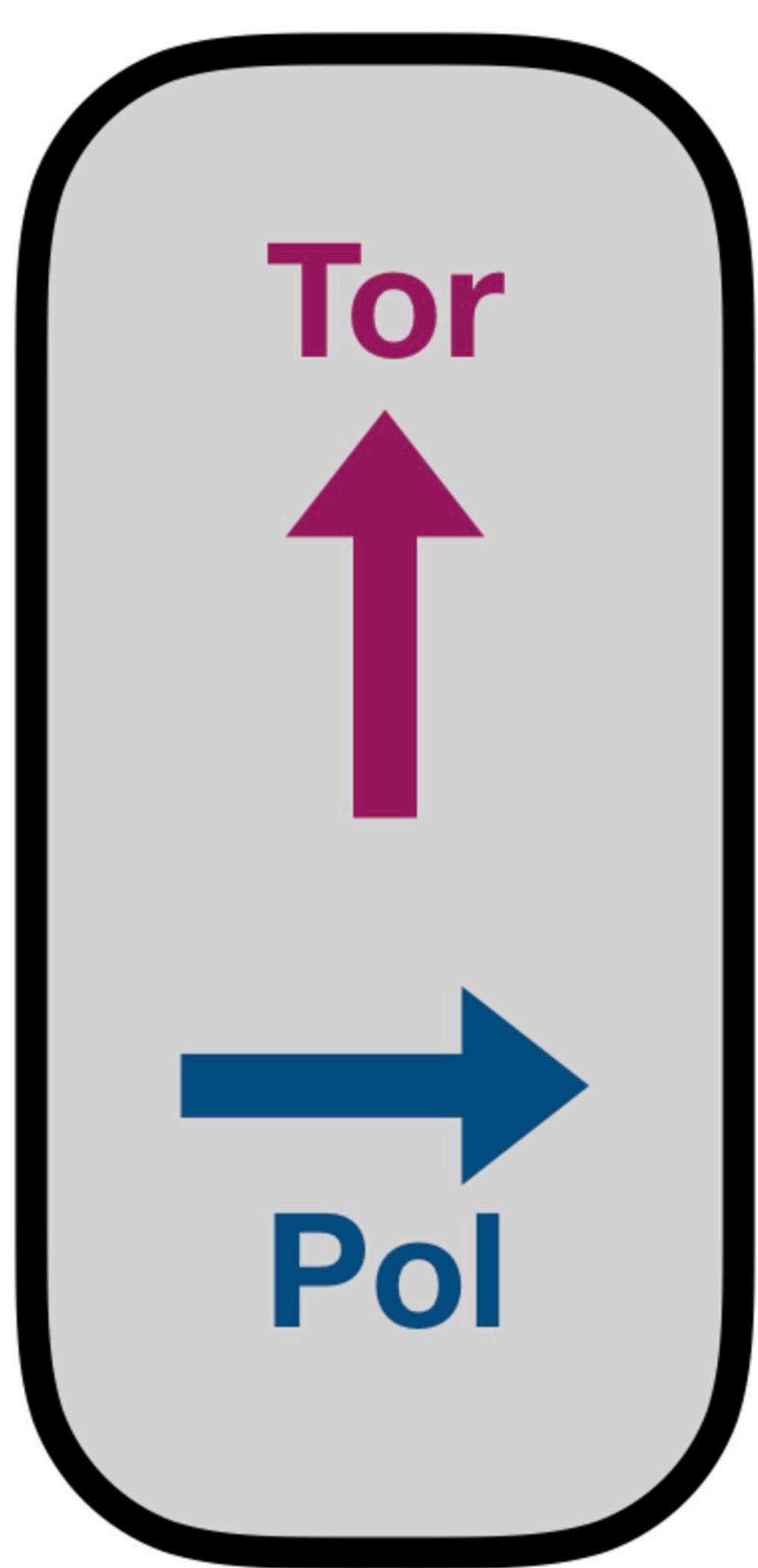
Side View



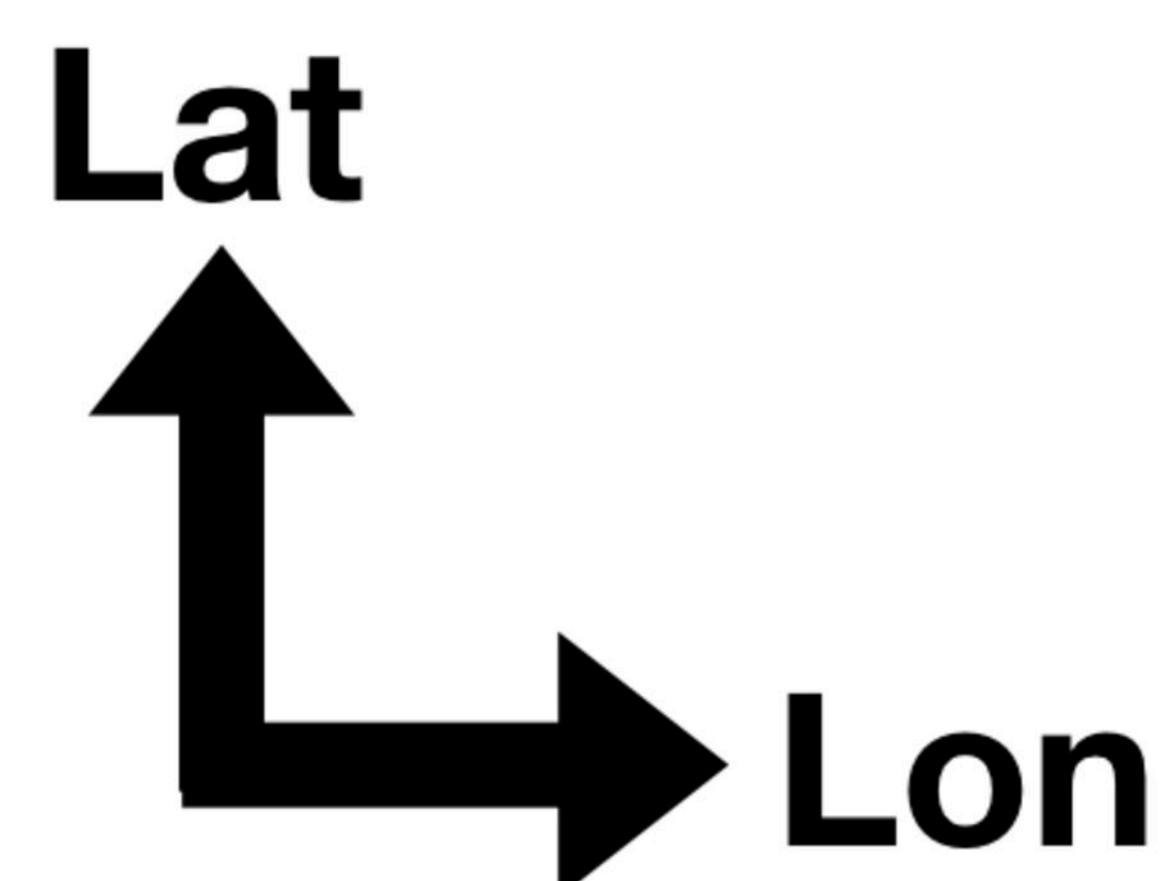
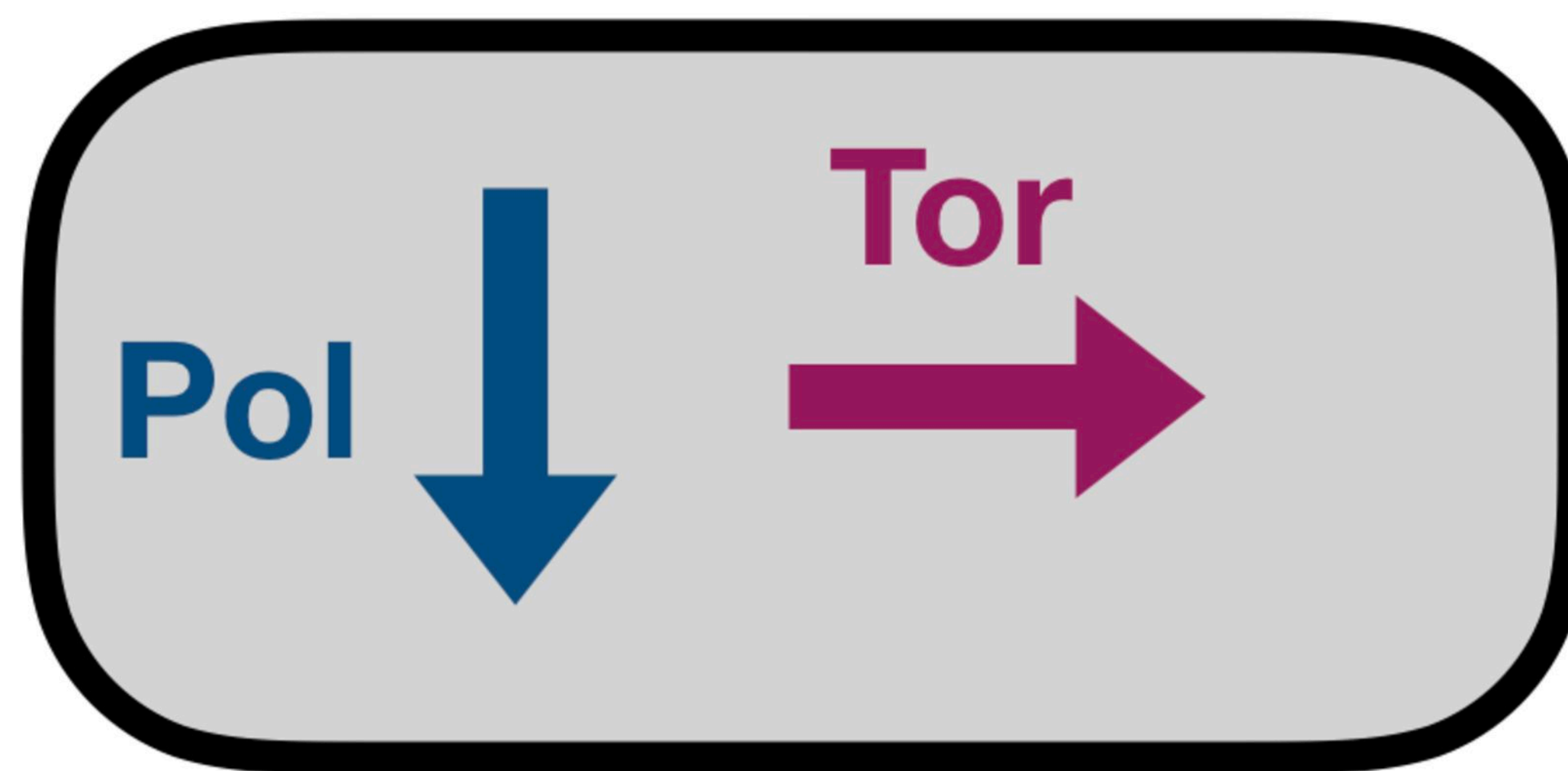
Front View



Vertical Orientation



Horizontal Orientation



Tilted Orientation

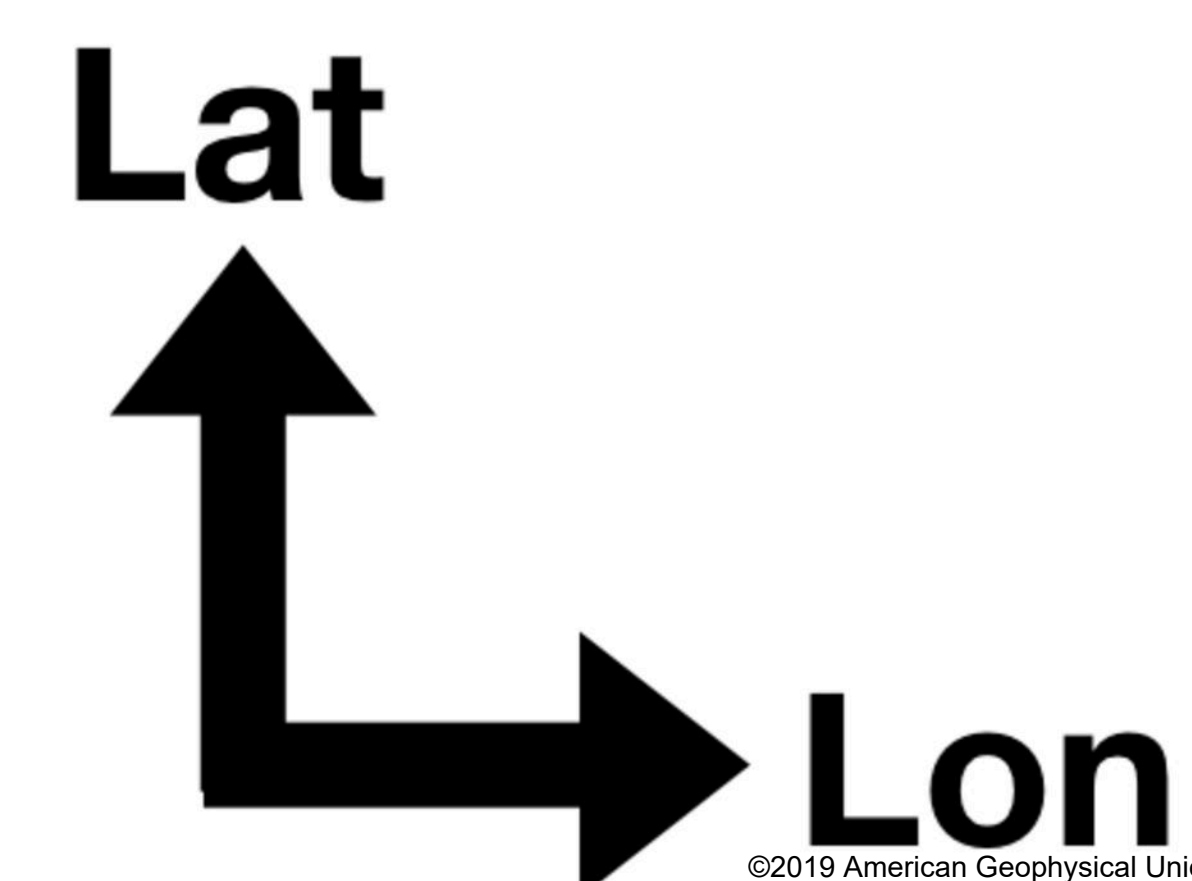
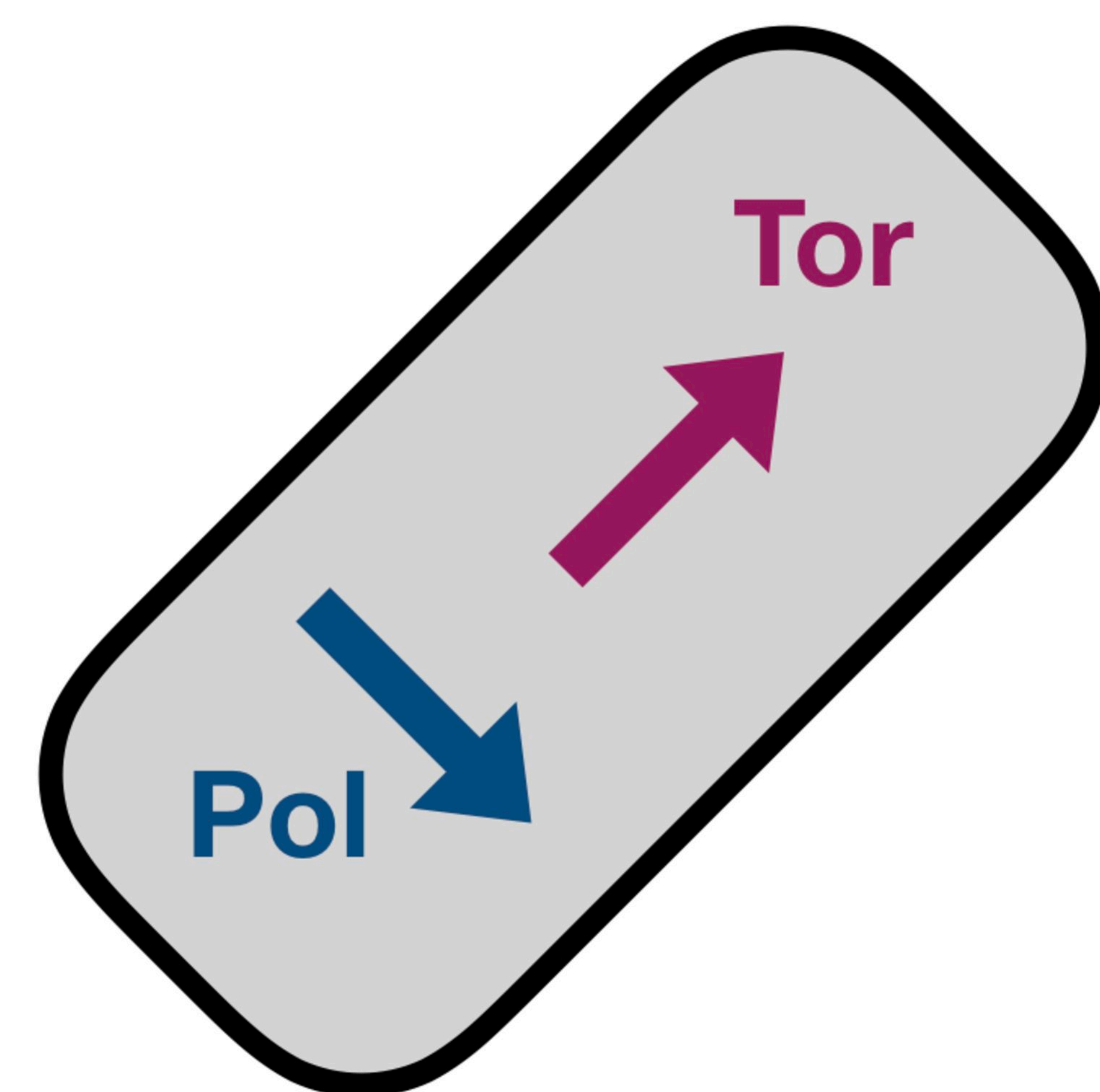


Figure 2.

Accepted Article

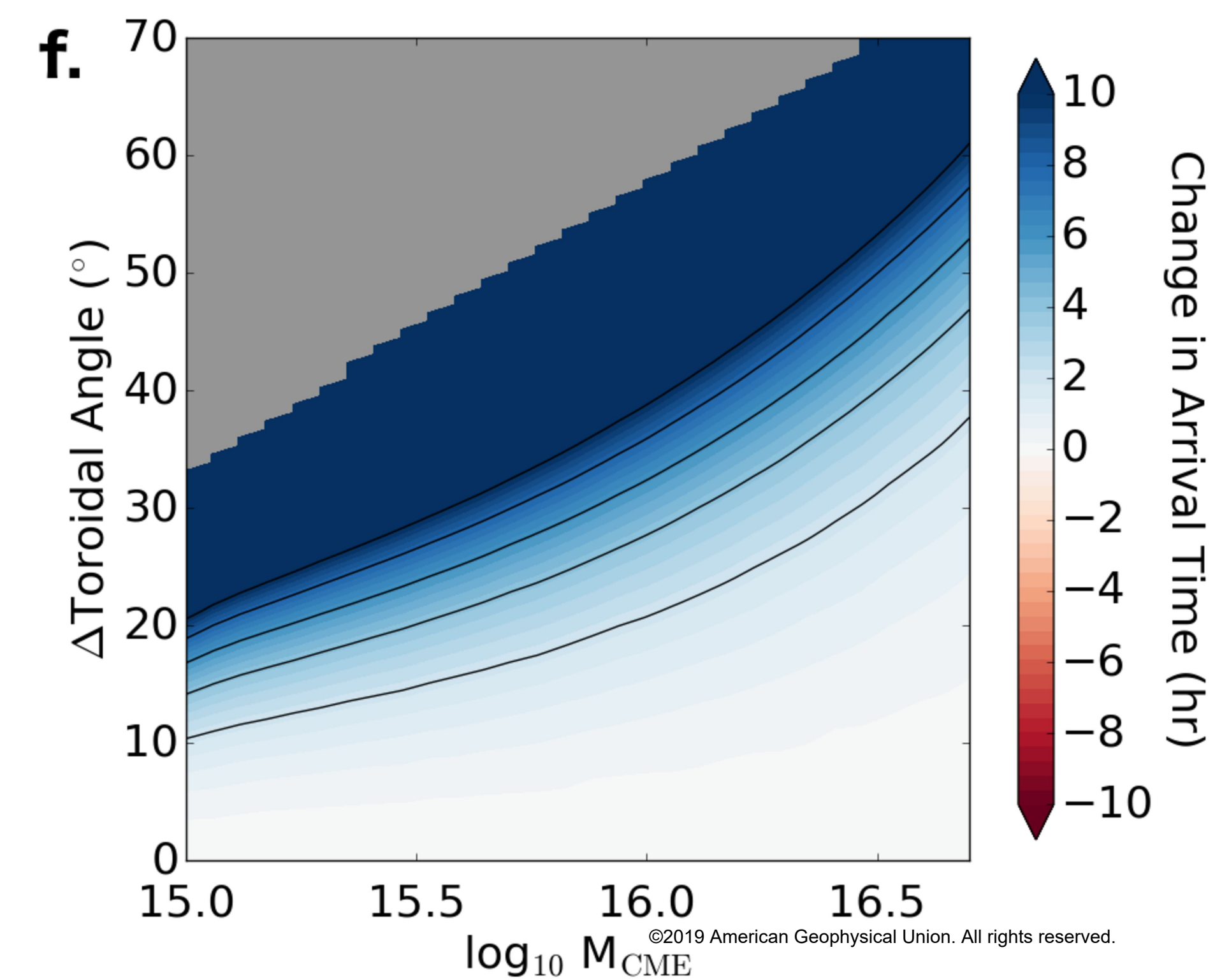
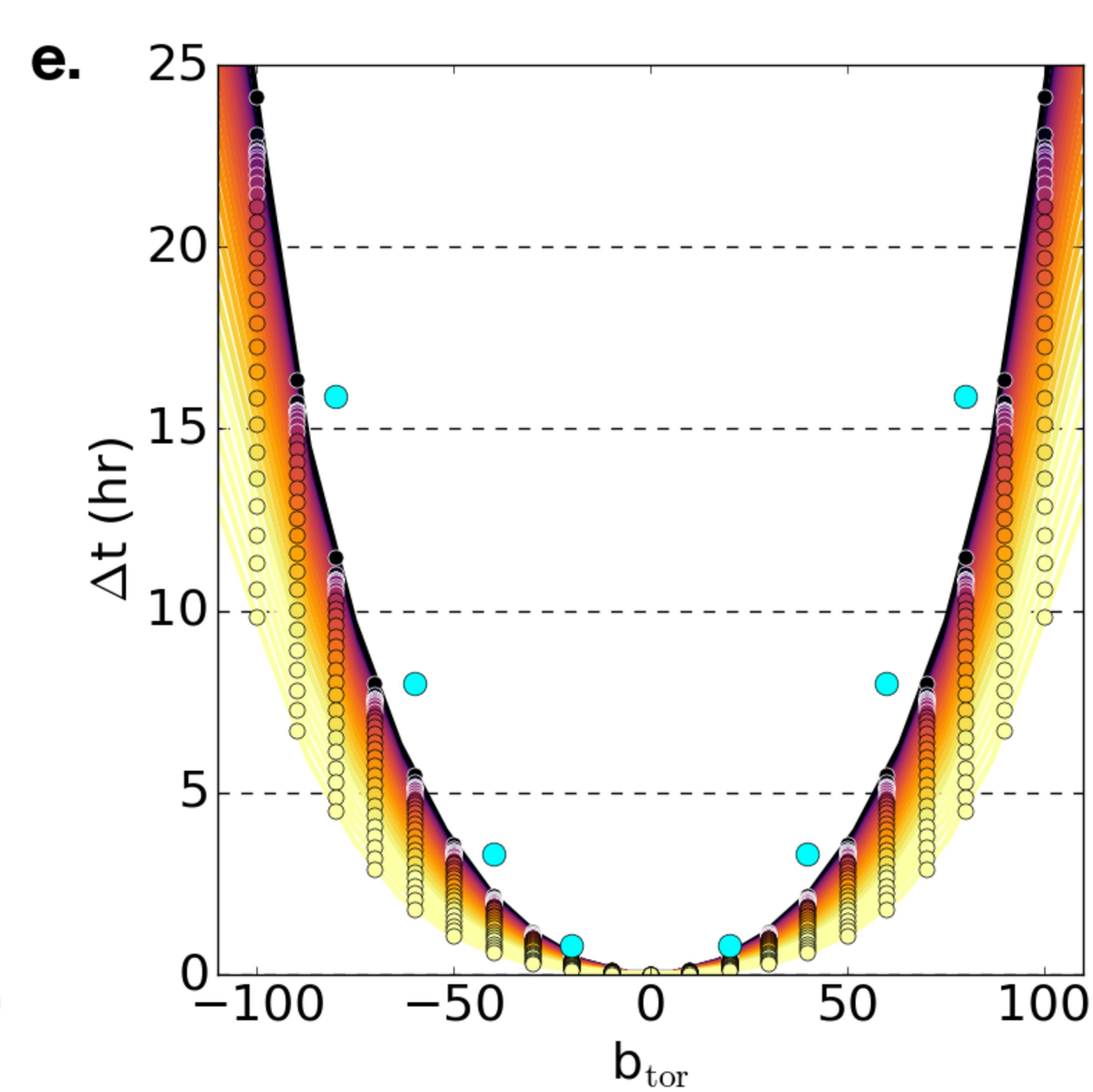
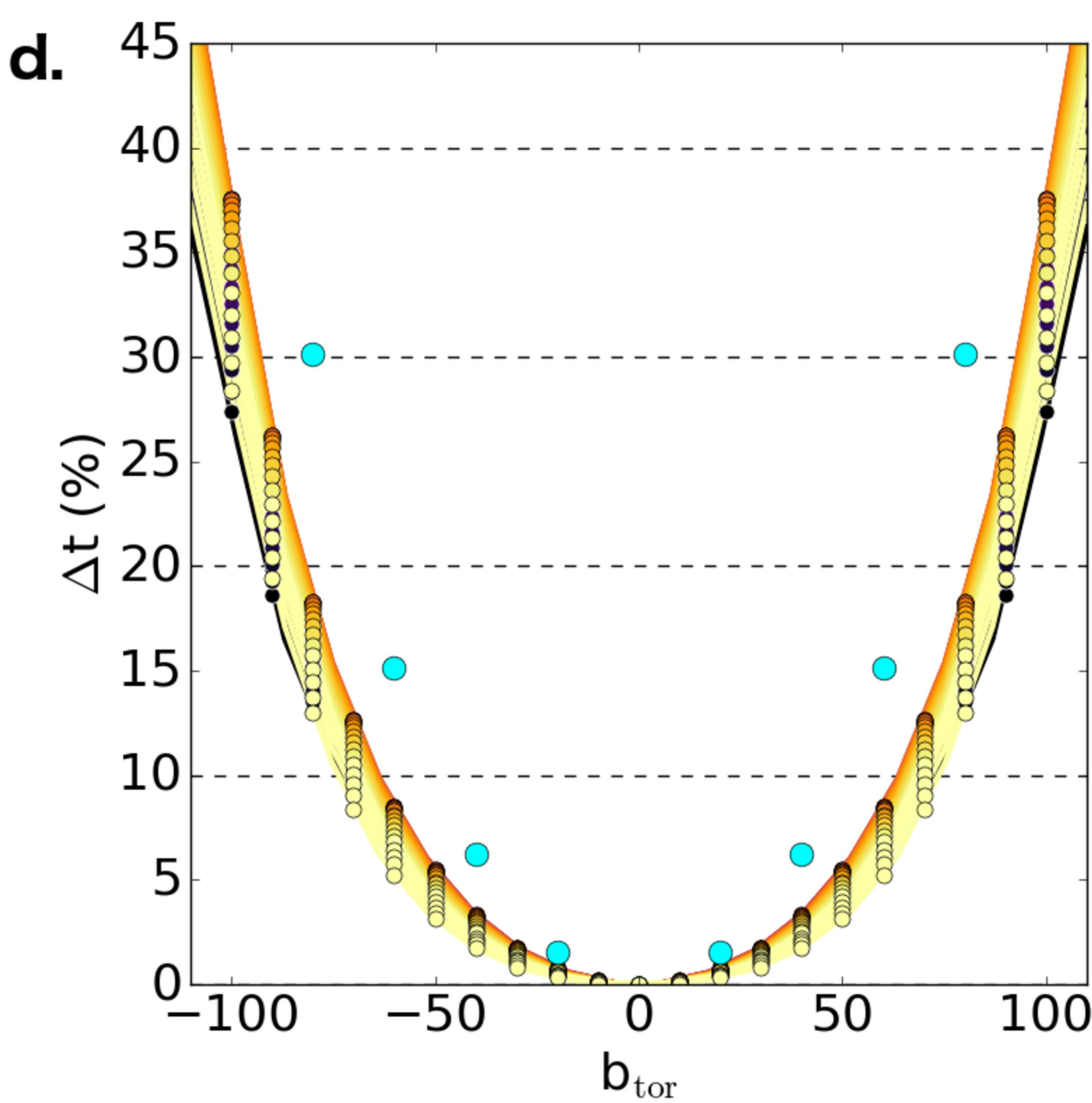
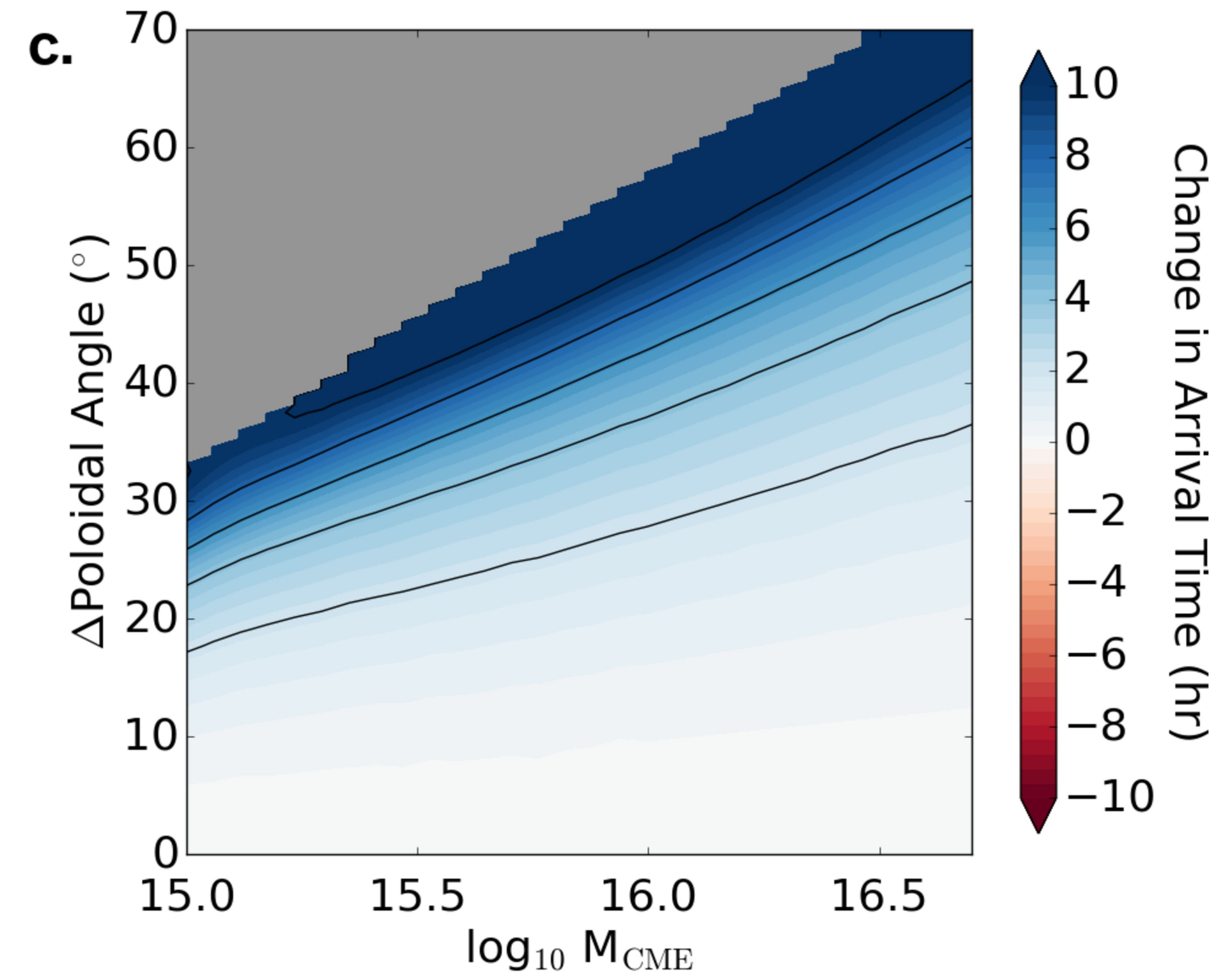
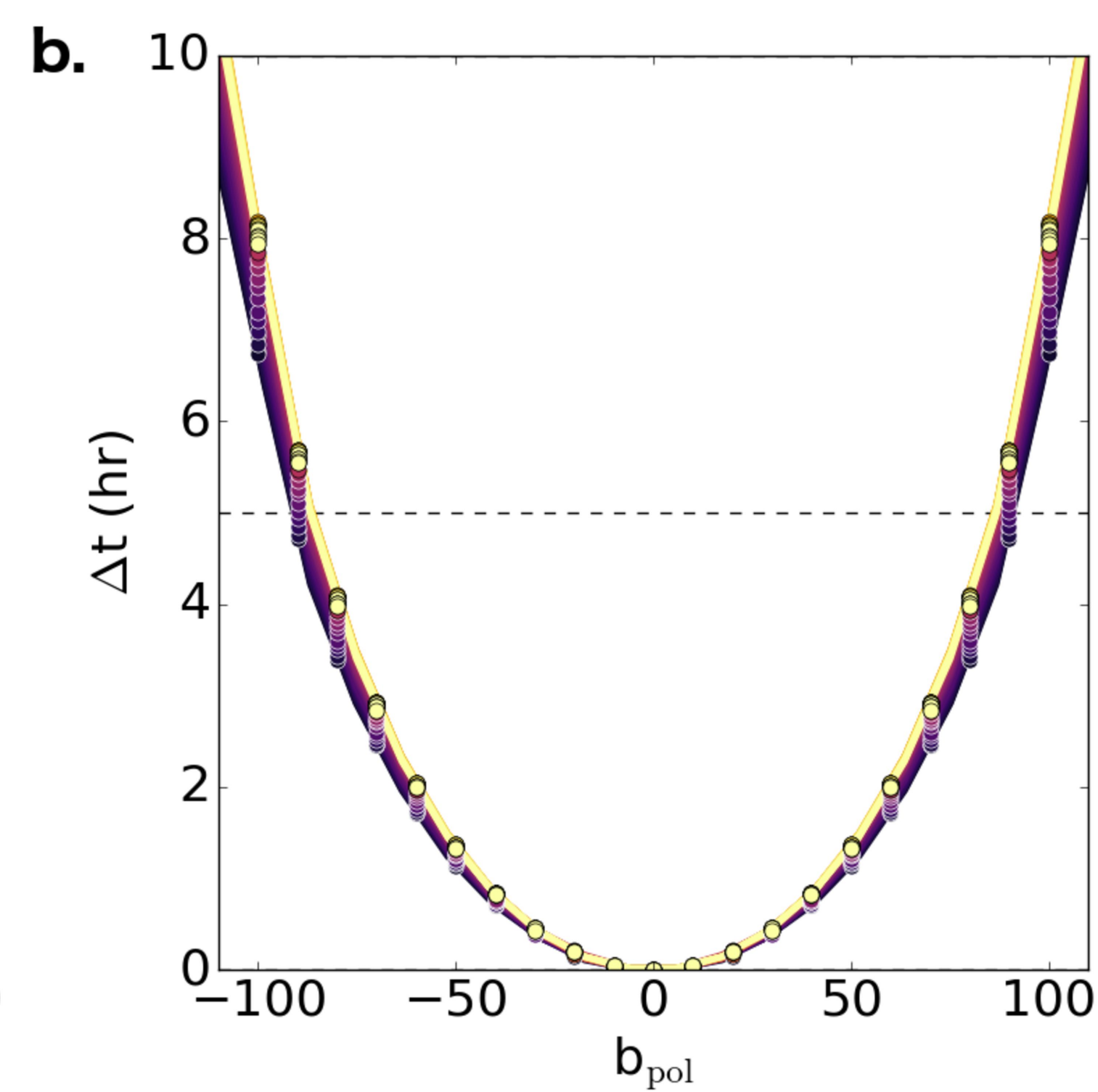
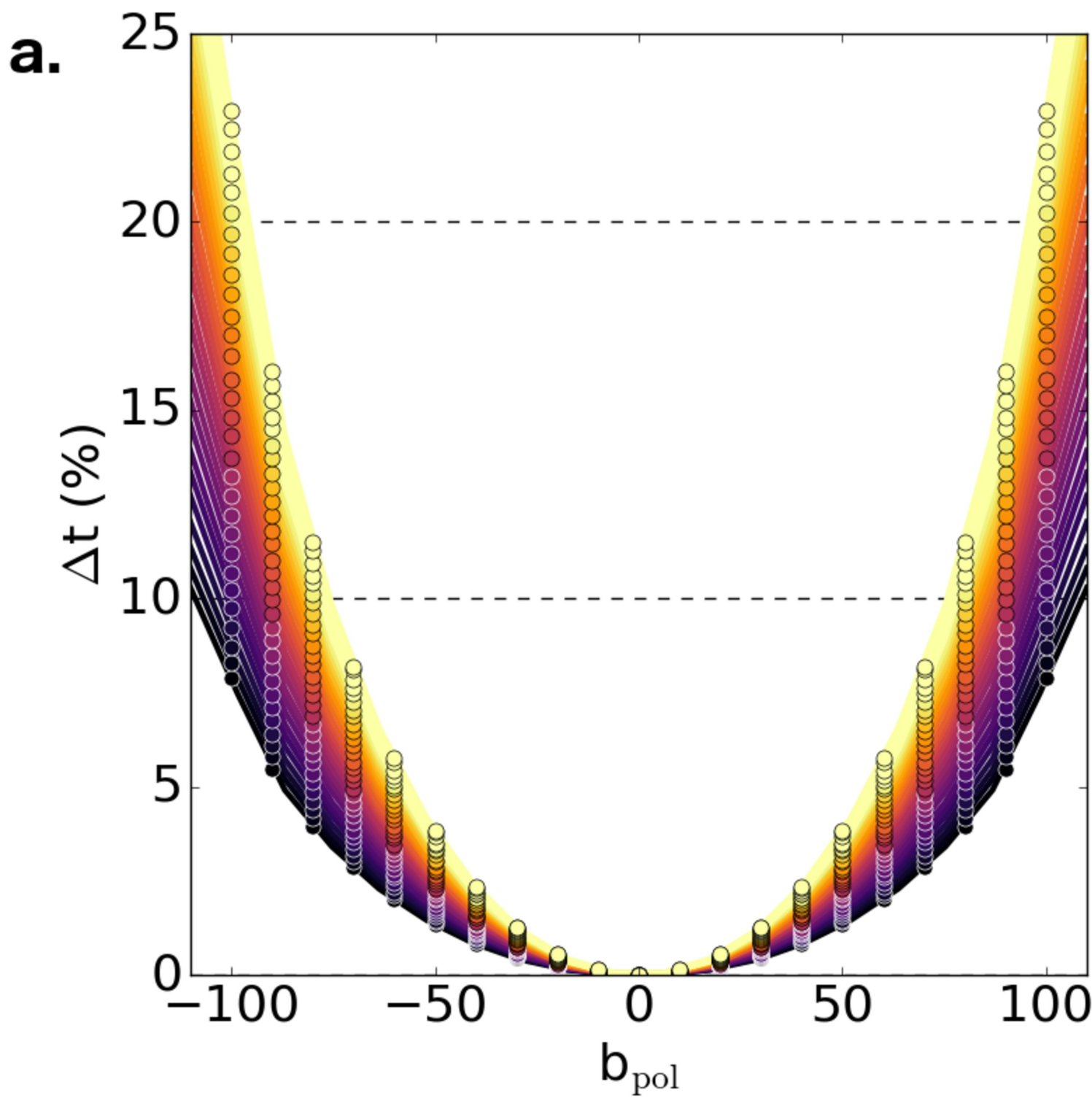


Figure 3.

Accepted Article

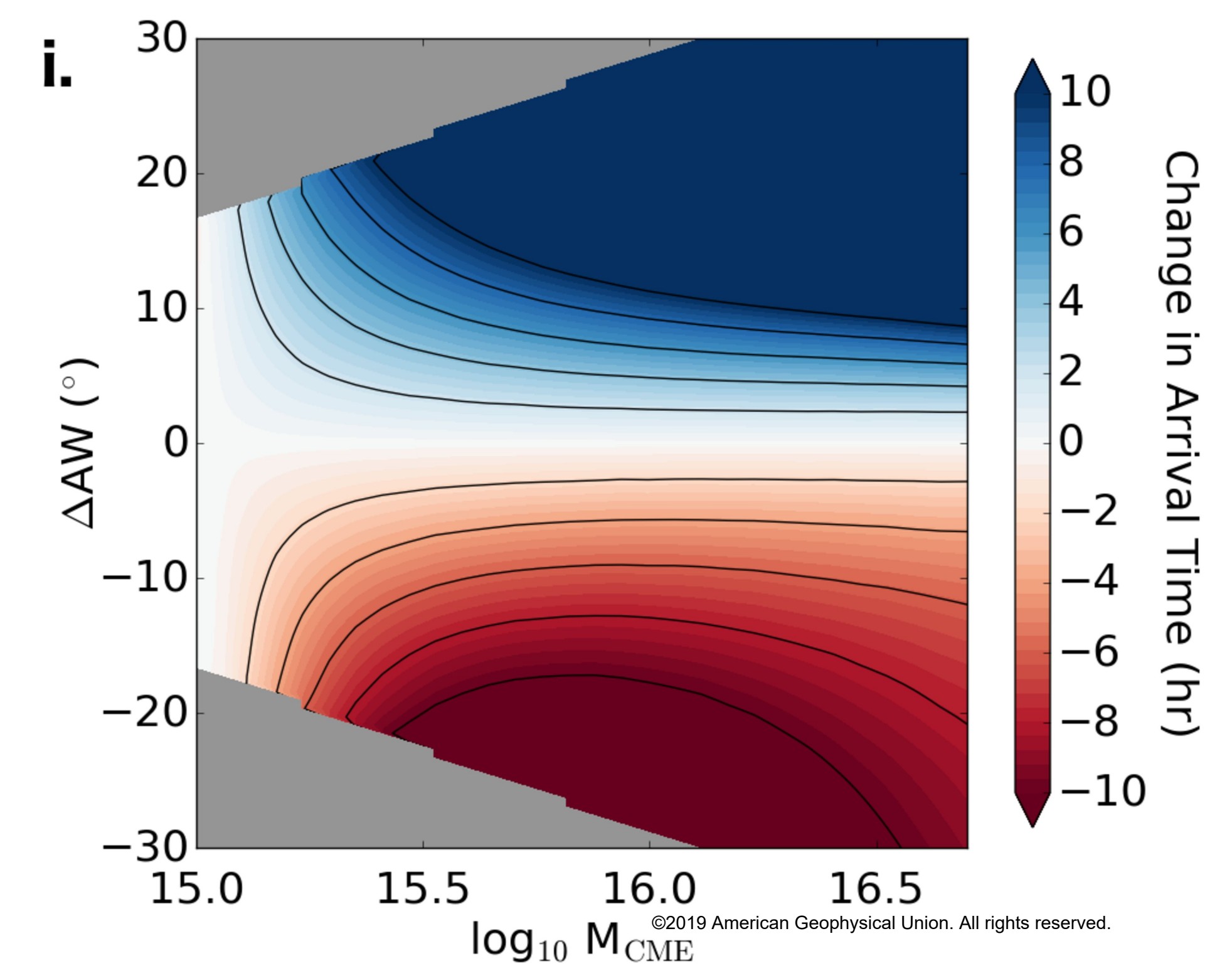
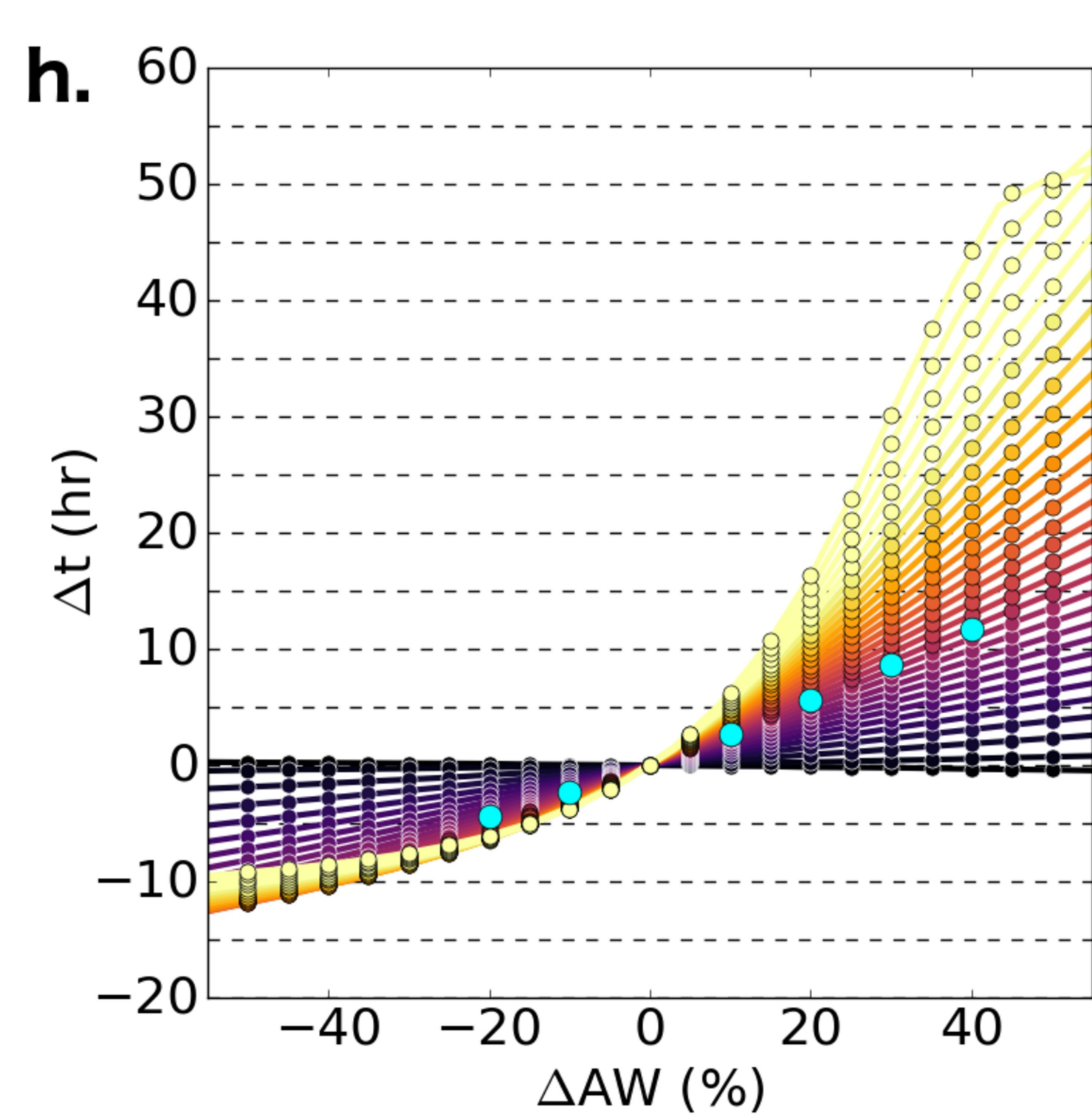
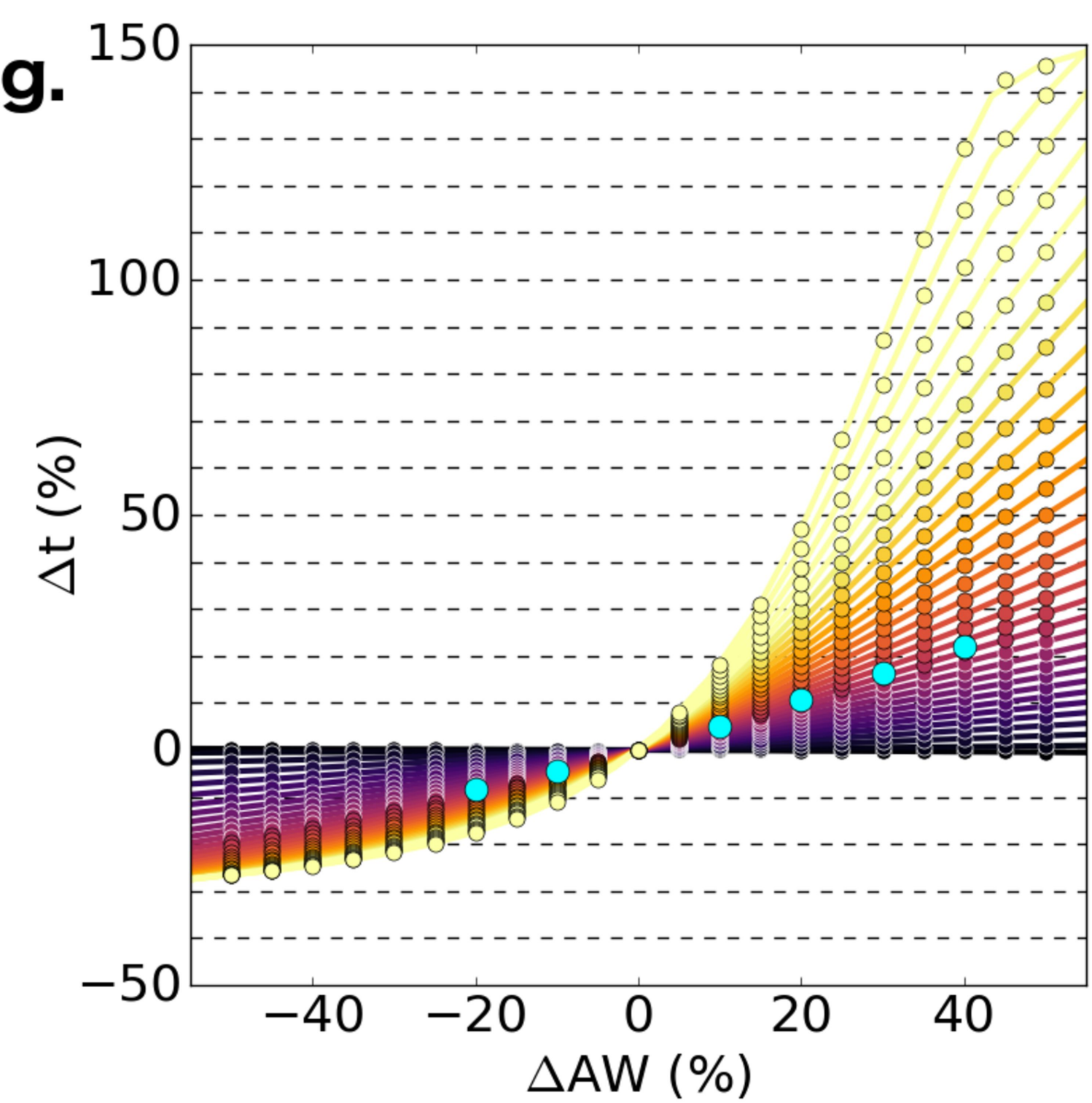
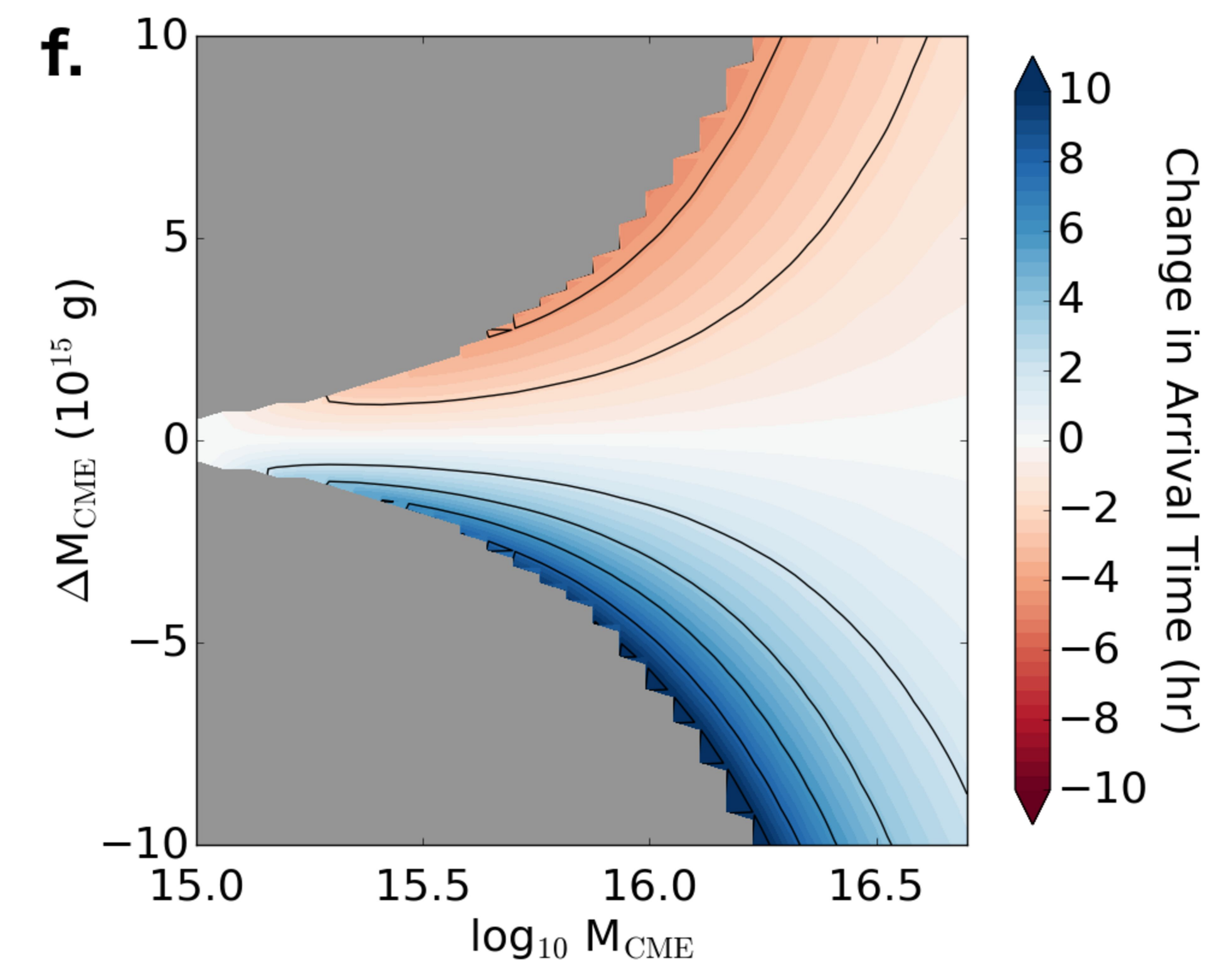
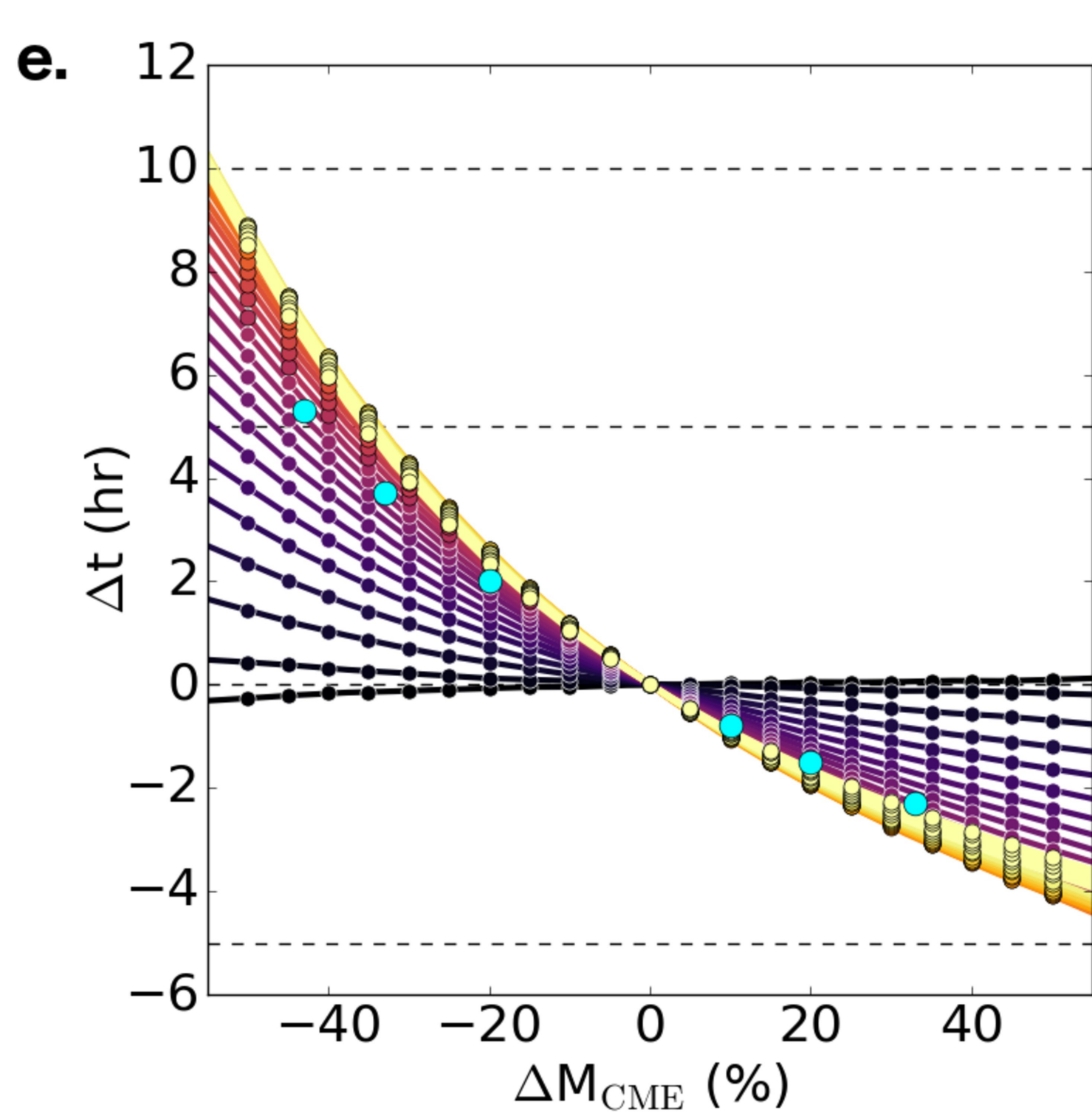
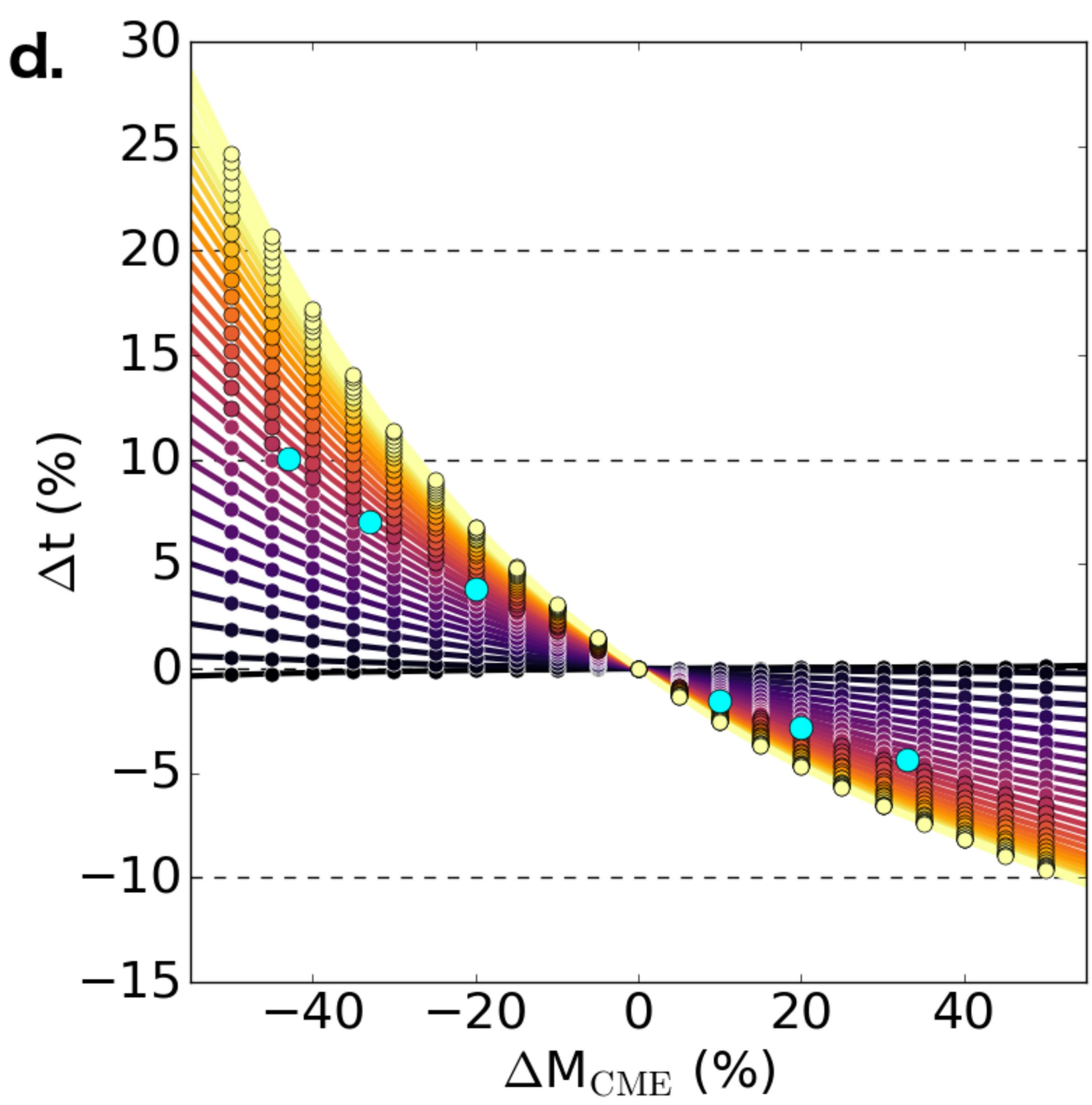
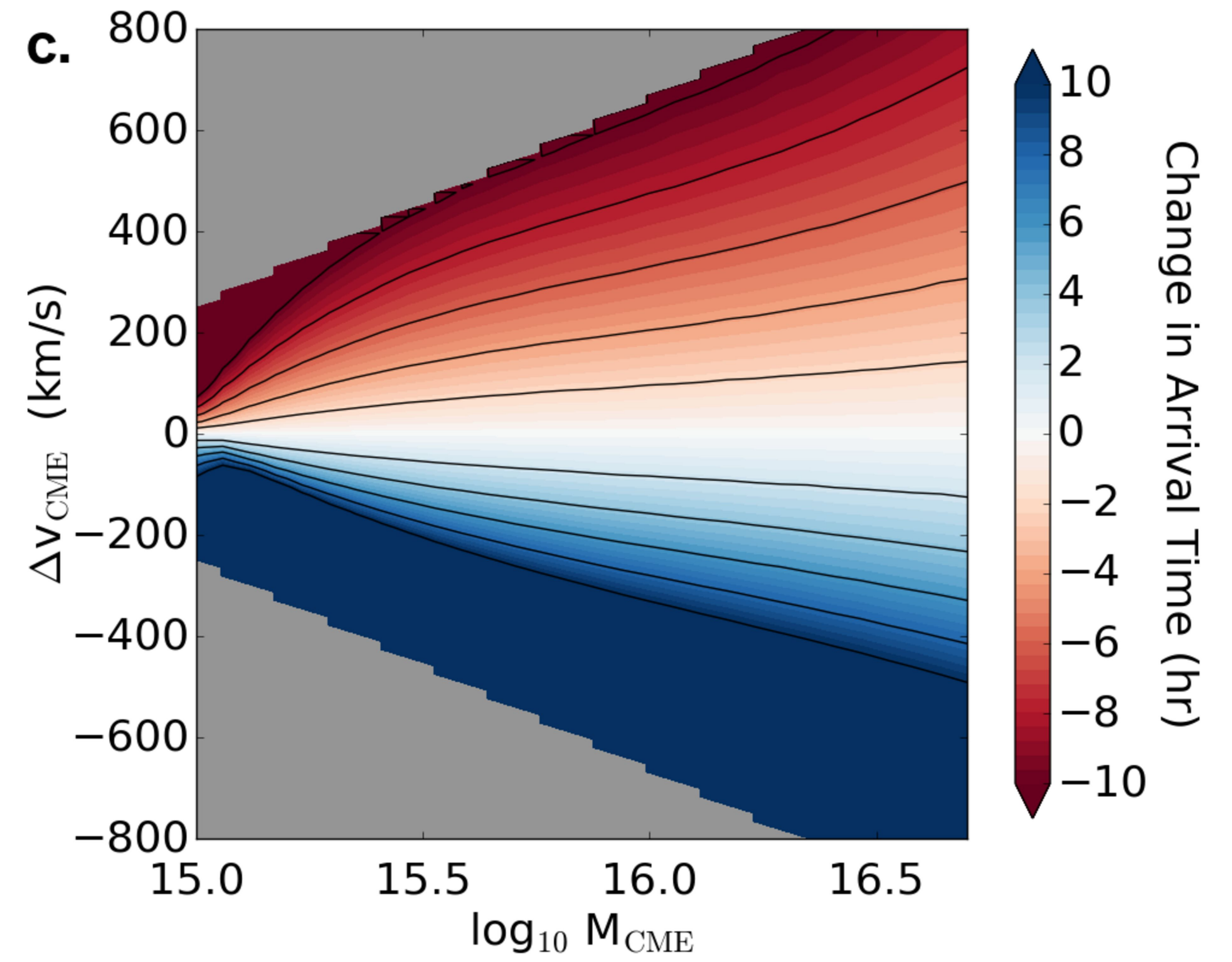
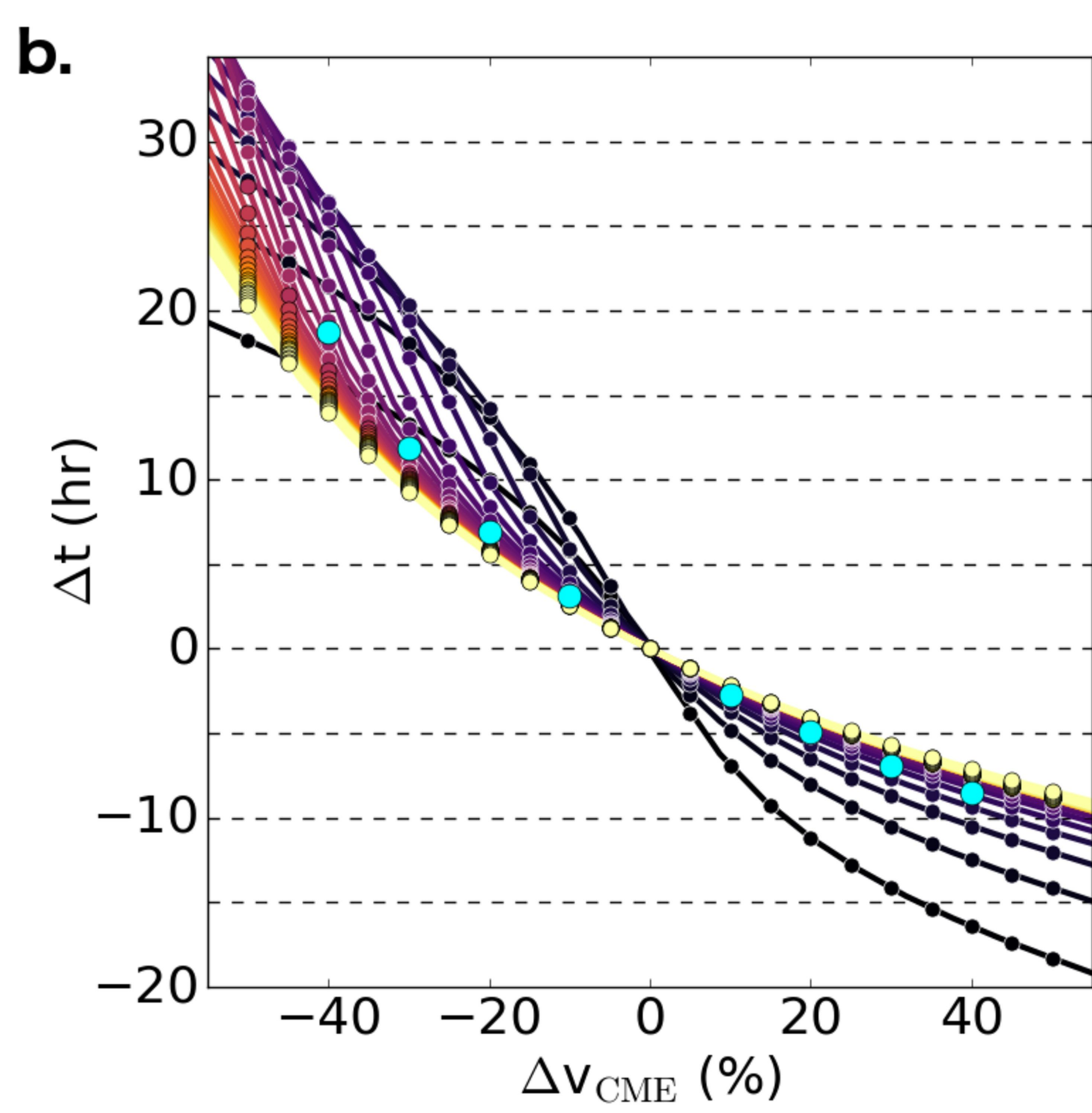
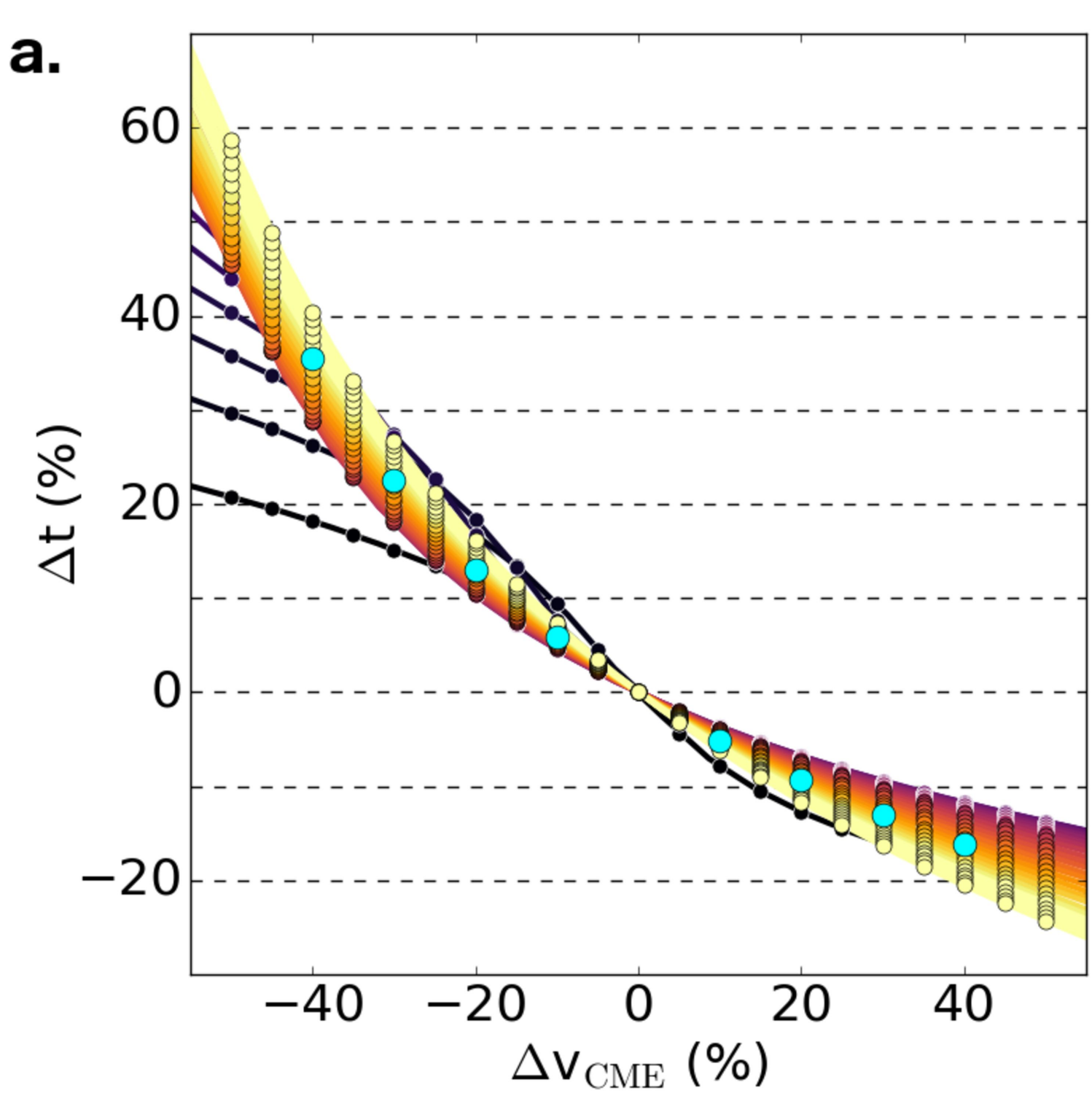


Figure 4.

Accepted Article

